The Meteoritical Society

*Meteoritics & Planetary Science* 58, Nr 7, 978–1001 (2023)
doi: 10.1111/maps.13990

# Silicon and iron isotopes in components of enstatite chondrites: Implications for metal–silicate–sulfide fractionation in the solar nebula

Jinia SIKDAR[1]*, Harry BECKER[1], and Jan A. SCHUESSLER[2]

[1]Institut für Geologische Wissenschaften, Freie Universität Berlin, Berlin, Germany
[2]Earth Surface Geochemistry, GFZ German Research Centre for Geosciences, Potsdam, Germany
*Corresponding author.
Jinia Sikdar, Institut für Geologische Wissenschaften, Freie Universität Berlin, Malteserstrasse 74-100, Berlin D-12249, Germany.
E-mail: jinia@zedat.fu-berlin.de; jiniasikdar10@gmail.com

*(Received 21 March 2022; revision accepted 17 April 2023)*

**Abstract**–Silicon and iron isotope compositions of different physically separated components of enstatite chondrites (EC) were determined in this study to understand the role of nebular and planetary scale events in fractionating Si and Fe isotopes of the terrestrial planet-forming region. We found that the metal–sulfide nodules of EC are strongly enriched in light Si isotopes ($\delta^{30}Si \geq -5.61 \pm 0.12‰$, 2SD), whereas the $\delta^{30}Si$ values of angular metal grains, magnetic, slightly magnetic, and non-magnetic fractions become progressively heavier, correlating with their Mg# (Mg/(Mg+Fe)). White mineral phases, composed primarily of $SiO_2$ polymorphs, display the heaviest $\delta^{30}Si$ of up to $+0.23 \pm 0.10‰$. The data indicate a key role of metal–silicate partitioning on the Si isotope composition of EC. The overall lighter $\delta^{30}Si$ of bulk EC compared to other planetary materials can be explained by the enrichment of light Si isotopes in EC metals along with the loss of isotopically heavier forsterite-rich silicates from the EC-forming region. In contrast to the large Si isotope heterogeneity, the average Fe isotope composition ($\delta^{56}Fe$) of EC components was found to vary from $-0.30 \pm 0.08‰$ to $+0.20 \pm 0.04‰$. A positive correlation between $\delta^{56}Fe$ and Ni/S in the components suggests that the metals are enriched in heavy Fe isotopes whereas sulfides are the principal hosts of light Fe isotopes in the non-magnetic fractions of EC. Our combined Si and Fe isotope data in different EC components reflect an inverse correlation between $\delta^{30}Si$ and $\delta^{56}Fe$, which illustrates that partitioning of Si and Fe among metal, silicate, and sulfidic phases has significantly fractionated Si and Fe isotopes under reduced conditions. Such isotope partitioning must have occurred before the diverse components were mixed to form the EC parent body. Evaluation of diffusion coefficients of Si and Fe in the metal and non-metallic phases suggests that the Si isotope compositions of the silicate fractions of EC largely preserve information of their nebular processing. On the other hand, the Fe isotopes might have undergone partial or complete re-equilibration during parent body metamorphism. The relatively uniform $\delta^{56}Fe$ among different types of bulk chondrites and the Earth, despite Fe isotope differences among their components, demonstrates that the chondrite parent bodies were not formed by random mixing of chondritic components from different locations in the disk. Instead, the chondrite components mostly originated in the same nebular reservoir and Si and Fe isotopes were fractionated either due to gas–solid interactions and associated changes in physicochemical environment of the nebular reservoir and/or during parent body processing. The heavier Si isotope composition of the bulk silicate Earth may require accretion of chondritic and/or isotopically heavier EC silicates along with cumulation of refractory forsterite-rich heavier silicates lost from the EC-forming region to form the silicate reservoir of the Earth.

## INTRODUCTION

Silicon and iron are among the most common rock-forming elements of the Earth with abundances of approximately 14% and 30% $g\,g^{-1}$, respectively (McDonough & Sun, 1995). Most of the Si budget of the Earth resides in its crust and mantle, which combined is referred as bulk silicate Earth (BSE). On the other hand, >90% of the planet's Fe inventory resides in the core of the Earth (Allègre et al., 1995; Palme & O'Neill, 2014). Seismic studies indicate that the Earth's core should contain ~6–10 wt% of light elements (Si, S, N, O, C) to explain its density deficit relative to pure Fe-Ni alloy (Birch, 1964). Among the light elements, silicon is argued to be a particularly important constituent of the core because of its unique siderophile behavior at conditions relevant to terrestrial core formation, that is, high temperature ($T > 2000$ K), high pressure (≥40 GPa), and low oxygen fugacity (Gessmann et al., 2001; Shahar et al., 2011). The super-chondritic Mg/Si ratio of BSE further suggests that Fe-Ni-Si alloy might form a major phase of the Earth's core (Allègre et al., 1995; Rubie et al., 2011; Wade & Wood, 2005). The distribution of Si and Fe in both metallic and silicate fractions of the Earth implies that the two elements must have remained in close association with each other during various stages of planetary accretion and differentiation. The redox reaction involving the coupling between Si and Fe to form Fe-Si alloy is given by the following Equation (Javoy et al., 2010):

$$SiO_{2(Silicate)} + 2Fe_{(Metal)} = Si_{(Metal)} + 2FeO_{(Silicate)} \quad (1)$$

Such processes involving mass transfer and redox reactions are often accompanied by changes in the bonding environment of Si and Fe. The resultant variation of bond strength among crystals, liquids, and gases can induce a shift in the stable isotope composition of Si and Fe, even at high temperature (Schauble, 2004; Sossi et al., 2016; Young et al., 2015). Therefore, comparing the distribution of stable isotopes of Si and Fe in BSE and chondritic meteorites (often considered as proxies of the building blocks of the Earth) forms a useful tracer of the accretionary and evolutionary history of terrestrial planets and their metallic cores.

A possible approach to provide constraints on the fractionation processes of the terrestrial planet-forming region is through the analyses of Si and Fe isotope composition in different components of enstatite chondrites (EC), which were accreted at shorter heliocentric distances compared to carbonaceous chondrites (CC) and ordinary chondrites (OC) (Kallemeyn & Wasson, 1986). EC are the most reduced group of meteorites whose mineral inventories are dictated by very low oxygen ($fO_2$) and high sulfur ($fS_2$) fugacities (El Goresy et al., 2017; Grossman et al., 2008). Due to formation under exceptionally reducing conditions, EC are the only naturally available undifferentiated meteorites that incorporates a substantial abundance of Si (up to 5 wt%) in their metallic phases (Horstmann et al., 2014; Ringwood, 1960), and thus, Si in bulk EC is partitioned between silicate and Fe-Ni metals (Weyrauch et al., 2018). Iron, on the other hand, is mostly distributed among the metallic (Fe-Ni) and sulfidic phases (troilite, FeS) of EC, and only a minor amount of FeO (<1 wt%) resides in its silicate fractions (Kallemeyn & Wasson, 1986).

The mass-dependent Si isotope composition ($\delta^{30}Si$, which expresses the deviation of sample's $^{30}Si/^{28}Si$ ratio relative to NBS-28 glass reference material in parts per 1000) of EC is significantly lighter compared to OC, CC, achondrites, and terrestrial and lunar basalts (Armytage et al., 2011; Fitoussi & Bourdon, 2012; Georg et al., 2007; Savage & Moynier, 2013; Zambardi et al., 2013). Additionally, the Mg/Si ratio of EC ($0.70 \pm 0.07$) is also lower than BSE ($1.20 \pm 0.02$), CC ($0.91 \pm 0.04$), and OC ($0.81 \pm 0.03$) (McDonough & Sun, 1995). The discrepancies between EC and BSE in terms of their overall chemical composition, Mg/Si ratio, and Si isotope composition have been used to argue against any major contribution of EC as Earth-forming materials (Fitoussi & Bourdon, 2012). This conclusion apparently contradicts evidence from mass-independent variations of oxygen and several metal isotopes in EC, which are similar to the Earth, and forms the basis for assuming that EC or similar materials played a major role in the formation of terrestrial planets (Dauphas, 2017; Javoy et al., 2010; Piani et al., 2020). A solution to this conundrum might be either (i) the mass-dependent Si isotope composition of EC or that of the Earth reflect processes that are decoupled from other isotope systems, or (ii) the mass-independent isotopic variations in meteorites are independent of their bulk chemical compositions, or alternatively (iii) there was more chemical variance in the solar system for a given mass-independent isotopic composition compared to the variance constrained by meteoritic record. A corollary of the last point is that the Earth and other terrestrial planets may contain materials that do not occur among the known planetary sample suite (Drake & Righter, 2002; Fischer-Gödde et al., 2020). Chondritic meteorites are composed of diverse components that typically reflect a multistage evolution of the proto-planetary disk (Scott & Krot, 2014), and therefore, it is difficult to constrain the origin of chondrites and their parent bodies using only whole rock isotope data. In situ Si isotope data (Kadlag et al., 2019) and Si isotope analyses in phases enriched in silicate and metallic fractions of EC (Savage & Moynier, 2013; Sikdar & Rai, 2020) indicate considerable Si isotope heterogeneity

within EC. For example, the reported $\delta^{30}$Si of EC silicates ranges from values similar to CC-OC and/or heavier whereas $\delta^{30}$Si of EC metals can be as low as −8‰ (Kadlag et al., 2019). Similarly, there are evidences of heterogeneous Fe isotope compositions (expressed as $\delta^{56}$Fe, which is per mill deviation of sample's $^{56}Fe/^{54}Fe$ ratio relative to IRMM-014 reference material) among the magnetic and non-magnetic (NM) fractions of EC, with $\delta^{56}$Fe ranging from $-0.34 \pm 0.04$‰ to $+0.20 \pm 0.07$‰ (Wang et al., 2014). Since both Si and Fe are major mineral-forming elements of EC, a combined study of Si and Fe isotopes in its different physically separated components is expected to provide insights into the physicochemical conditions and kinetics of gas–solid interaction processes that prevailed in the reduced planet-forming region of the inner solar system. So far, combined high precision Si and Fe isotope data from the same components of EC are not available, and hence, the origin of Si and Fe isotope heterogeneity in EC has remained poorly constrained. In the present contribution, we have attempted to address the possible nebular and planetary scale pathways through which the reduced inner solar system materials (akin to EC parent bodies) were accreted by analyzing Si and Fe isotope composition of a spectrum of different physically separated components of EC.

## SAMPLES AND ANALYTICAL METHODS

The chondritic components analyzed for Si and Fe isotope composition were obtained from two EH3 chondrites (Sahara 97072 and Kota-Kota, both are finds), one EH4 chondrite (Indarch, Fall), one EH4 impact melt breccia (Abee, Fall), and one EL3 chondrite (MAC 88184, Find). Silicon and Fe isotope analyses were also carried out in bulk meteorite fractions and magnetic phase separates of an ungrouped chondrite (NWA 5492, Find). Additionally, Fe isotope analyses were performed on the whole rock and magnetic fractions of two OC (WSG 95300 and QUE 97008) to understand isotope fractionation in planetary bodies that were formed at relatively higher oxygen fugacity (IW − 2 to IW + 1, where "IW" stands for iron–wüstite buffer) compared to that of EC (IW − 5.8 to IW − 6.6) (Cartier et al., 2014).

The chondrites were first broken into pieces using a mortar–pestle set made of diamonite (i.e., composed of synthetic $Al_2O_3$) and any visible weathered or rusty materials were removed. The larger pieces of the EH3 chondrites, that is, Kota-Kota and Sahara 97072, weighing ~1 g were crushed, and their various components were physically separated under a binocular microscope. Metals in the least equilibrated EH3 chondrites occur in two dominant textural forms, that is, rounded metal–sulfide nodules (MSNs) and angular metal grains (AMGs). MSN are round to subround, concentrically layered objects of typically ~50 to 800 μm in size and are dominantly composed of Si-bearing kamacite (α-(Fe,Ni)), perryite $(Ni,Fe)_5(Si,P)_2$, troilite (FeS) with minor fractions of other phases such as niningerite (MgS), daubréelite ($FeCr_2S_4$), schreibersite ($(Fe,Ni)_3P$), sinoite ($Si_2N_2O$), graphite (C), enstatite ($MgSiO_3$) etc. (El Goresy et al., 2017). Two size fractions of MSN were considered in the present study, that is, >250 μm and <250 μm. AMGs represent angular to subangular isolated grains of metals found in close association with MSNs, with size varying from ~50 to 100 μm. White mineral phases (WMPs) are referred to the fine-grained, bright white-colored, inherently non-magnetic mineral phases found mostly in the matrices of unequilibrated (EH3) EC. Enstatite and cristobalite comprise approximately 45 and 30 vol% of the non-magnetic mineral phases in the matrices of EH3 chondrites (Lehner et al., 2014). The examination of physical and optical properties of WMPs (milky white color, brittle tenacity, and vitreous luster) hints that cristobalite or other $SiO_2$ polymorphs might represent the main constituent of WMPs. We have examined the Si isotope composition of such WMPs for the first time in this study. Owing to the predominant sizes and distinct textures of MSNs, AMGs, and WMPs, we were able to sample these components from broken meteorite sections after their visual inspection under a binocular microscope. Plastic tweezers were used to mechanically pick up MSNs, AMGs, and WMPs. Matrix materials attached to the studied components were removed as much as possible to limit the risk of contamination.

A separate piece of Kota-Kota, Sahara 97072, and whole rock pieces of all other chondrites (weighing ~300–400 mg) were crushed into fine homogeneous powder using diamonite mortar and pestle. One fraction of the well-mixed powdered samples was considered a representative of the bulk meteorite (BM) composition whereas the other part was further separated into magnetic (M), slightly magnetic (SM), and non-magnetic (NM) fractions using a hand magnet based on decreasing magnetic susceptibility. The magnetic fractions were predominantly composed of metals, which might be derived partly from MSNs, AMGs, and fine-grained metals intergrown with sulfides and minor silicates. Since such magnetic fractions are mostly derived from metals found dispersed in the matrices of chondrites, we have referred these magnetic phases as matrix metals. The SM and NM fractions, on the other hand, were mostly composed of matrix silicates, silicate clasts, chondrule fragments, and sulfides with minor and negligible metal content, respectively. Figure 1 provides a flow chart describing the different chondrite components analyzed in this study.

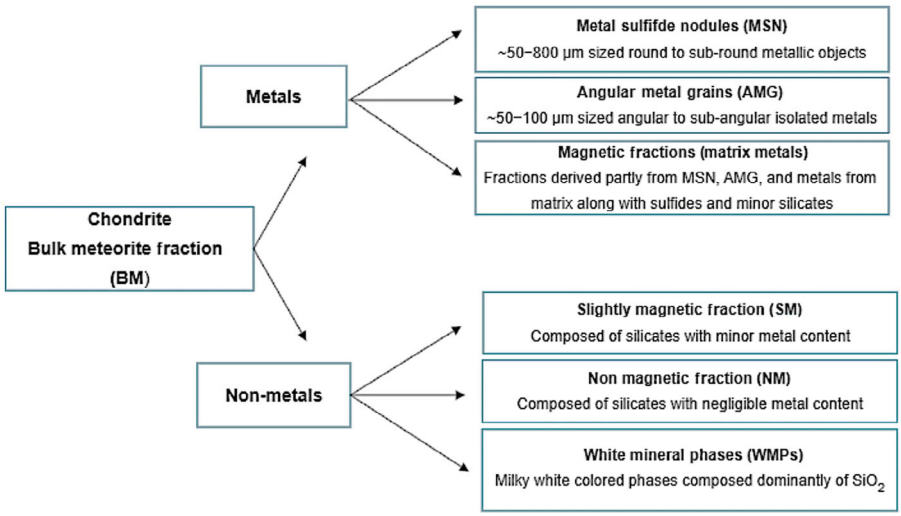


FIGURE 1. Flow chart describing the different chondrite components considered in this study. (Color figure can be viewed at wileyonlinelibrary.com)

The different fractions of chondritic components were further separated into two aliquots for their respective Si and Fe isotope analyses. Sample digestion and purification of Si and Fe by ion exchange column chromatography were carried out at Freie Universität Berlin. High precision Si and Fe isotope analyses were performed using a Thermo Scientific Neptune Plus Multi-Collector Inductively-Coupled-Plasma Mass Spectrometer (MC-ICPMS) at the German Research Centre for Geosciences (GFZ), Potsdam following established protocols (Oelze et al., 2016; Schoenberg & von Blanckenburg, 2005). Aliquots of the digested solutions (in 0.3 M $HNO_3$ and doped with 1000 ppm Cs) were analyzed by inductively coupled optical emission spectrometry (ICP-OES, Varian 720-ES) to determine major element concentrations in sample solutions. The elements of interest, that is, Mg, Fe, Ni, and S were measured at wavelengths of 279.5, 238.2, 216.5, and 181.9 nm, respectively. USGS rock standard BHVO-2 was used for calibration. The dilution factor of the samples was kept at 16. Blank contribution of the elements of interest was typically lower than 30 ng. We have not weighed the chondrite components to avoid contamination while handling their small volume, and therefore, we have not reported their mass fractions in this study. Instead, elemental ratios such as Mg/(Mg+Fe) and Ni/S have been used to provide an estimate of the relative contributions of silicate, metal, and sulfide phases in the studied chondritic components.

## Sample Preparation and Mass Spectrometry for Si Isotope Analyses

The finely powdered samples were digested in 22 mL teflon vials (Savillex™) using a modified alkali flux digestion technique (Sikdar & Rai, 2017). Approximately 0.2–1.0 mg of finely homogenized sample powder was mixed with ~60–80 times the sample weight of suprapure NaOH flakes in digestion vial. The sealed vial was heated at ~190°C on a hot plate for ~48 h. After cooling, ~1 mL Milli-Q was slowly added to the flux–sample mixture with subsequent addition of approximately 2 mL concentrated HCl. The volume and proportions of HCl and MQ were adjusted in such a way that the pH of the solution prior to loading on the ion exchange column was ~1.5. The sample solution was subsequently ultrasonicated, allowed to cool to room temperature, and left undisturbed to equilibrate for at least 18 h.

Chromatographic purification of Si from reference materials (NBS-28, Diatomite, Big-Batch, BHVO-2), BM, and NM fractions of chondrites was carried out following published procedures (Georg et al., 2006; Oelze et al., 2016; Sikdar & Rai, 2017; Zambardi & Poitrasson, 2011) using 2 mL BioRad cation-exchange resin AG 50W-X12 (200–400 mesh, $H^+$ form) filled in BioRad poly-prep columns (10 mL reservoir volume and 2 mL bed volume). The resin was precleaned by rinsing with MQ, 3 M HCl, 6 M HCl, 7 M $HNO_3$, and 10 M HCl. Samples containing ~3–10 µg of Si (in diluted NaOH-bearing hydrochloric digestion solution at pH 1.5) were loaded on the resin and Si was eluted using 7–8 mL of Milli-Q at neutral pH (Georg et al., 2006). The purified Si solution was acidified to yield 0.1 M HCl solution for mass spectrometry. In order to use the $^{25}Mg/^{24}Mg$ ratio for mass bias drift correction, Mg solution from Alfa Aeser Specpure (evaporated and dissolved in 0.1 M HCl) was added to both sample and the bracketing standard for obtaining an Si:Mg mass ratio of 1:1. Before isotope analyses, quantitative recovery of Si (column yield

>98%) and purity of the sample solutions (>97% Si) were checked by ICP-OES analysis. The total procedural blank (from dissolution and column chemistry) was below the ICP-OES detection limit, that is, <20 ng Si compared to typical Si sample amounts of 4.5–10 µg. Owing to the high Fe-Ni content of EC metals, chromatographic purification of Si from magnetic fractions of EC was modified in the present study, which is detailed in the next section.

For Si isotope analyses, the sample and standard solutions (in 0.1 M HCl) were introduced into Neptune MC-ICPMS using an ESI APEX-Q desolvator. Jet sample and H skimmer cones were used. Ion optics was operated in medium resolution mode with a mass resolving power of ~7500 (m/Δm as defined by the peak edge width from 5% to 95% full peak height) to resolve Si signals from isobaric interferences of N-O molecules. The measurement of Si isotope ratios was performed in multidynamic mode (magnet jump alternating between Si and Mg isotopes), whereby instrumental mass bias was corrected using sample-standard bracketing (with NBS-28 as bracketing standard and 0.1 M HCl as blank solution) and internal standardization using Mg doping. The concentrations of both Si and Mg in samples and standards (0.6 µg $mL^{-1}$ for both Si and Mg) were matched to <5% difference. The $^{28}Si$ and $^{24}Mg$ signal intensities reached ~11 and ~20 V, respectively, with an acid background of <20 mV on $^{28}Si$. Si isotope measurements were obtained in 30 cycles of data acquisition with an integration time of 4 s per cycle, and each sample was measured at least three times during the sequence. The typical precision for Si isotope measurements based on $n = 30$ cycles of individual standard–sample–standard bracketing measurement was better than ±0.10‰ (2SD) for $\delta^{30}Si$ ($^{30}Si/^{28}Si$) and ±0.07‰ (2SD) for $\delta^{29}Si$ ($^{29}Si/^{28}Si$). Based on repeat sample dissolutions and measurements of reference materials, the long-term reproducibility of Si isotope analyses at GFZ has been estimated to be ±0.11‰ (2SD) on $\delta^{30}Si$ and ±0.08‰ (2SD) on $\delta^{29}Si$. The robustness of our analytical and measurement protocol for Si isotope measurements was checked by the accuracy of the following well-characterized reference materials: Diatomite, Big-Batch, RGM-2, and BHVO-2. Our results for $\delta^{30}Si_{Diatomite} = +1.13 \pm 0.12‰$, $\delta^{30}Si_{Big\text{-}Batch} = -10.67 \pm 0.14‰$, $\delta^{30}Si_{RGM\text{-}2} = -0.34 \pm 0.03‰$, and $\delta^{30}Si_{BHVO\text{-}2} = -0.27 \pm 0.11‰$ are in good agreement with the published values of these secondary standards (Armytage et al., 2011; Oelze et al., 2016; Zambardi & Poitrasson, 2011).

### *Modified Column Chromatography for Purification of Si from Metals*

Despite the simple matrix of EC metals (predominately Fe, Ni, S, and Si), it is not straightforward to purify Si from metal-rich fractions of EC via the traditional single-step cation exchange chromatography because the removal of excessive Fe-Ni matrices requires repetition of the column chemistry several times. In this study, we modified the chromatographic protocol for purification of Si from metals by using 3 mL AG 50W-X12 (200–400 mesh, $H^+$ form) cation exchange resin in 7.5 mL Spectrum®104704 polypropylene columns (referred here as "long column"). The resin was preconditioned with 3 M HCl, 6 M HCl, 7 M $HNO_3$, 10 M HCl, and MQ. Subsequently, purified Si was eluted using 15–30 mL MQ. Owing to the narrower column geometry, higher aspect ratio, and slower flow rate, separation of Si from metal-rich matrices was found to be more effective through the long column (LC) and clean Si was typically obtained after two or three column passes.

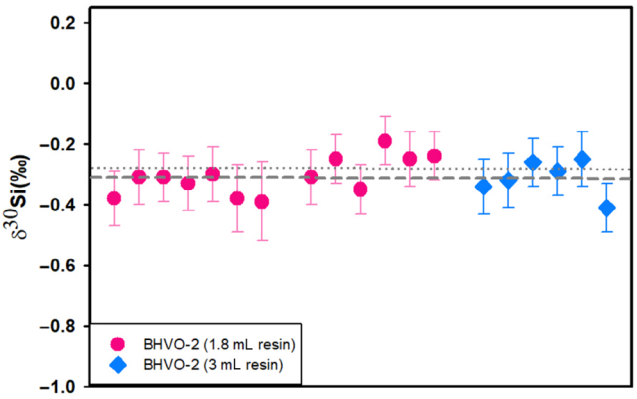


FIGURE 2. Plot shows good agreement between Si isotope composition of BHVO-2 purified using long column (3 mL resin volume) with the $\delta^{30}Si$ value of BHVO-2 purified via traditional column (1.8 mL resin volume), thereby demonstrating the robustness of our modified protocol to purify Si from metals. Error bars represent 2SD of individual measurement. The medium-dashed line represents the average $\delta^{30}Si$ of BHVO-2 purified by long column ($\delta^{30}Si = -0.31 \pm 0.12$) and the dotted line represents the published Si isotope composition of BHVO-2 ($-0.27 \pm 0.10$) by Savage et al. (2010). (Color figure can be viewed at wileyonlinelibrary.com)

Aliquots of BHVO-2 purified via LC chemistry yielded mean $\delta^{30}Si_{BHVO2\text{-}LC} = -0.31 \pm 0.12‰$, which is in good agreement with the Si isotope composition of BHVO-2 purified via traditional column chemistry obtained in this study ($-0.30 \pm 0.10‰$) and its published value of $-0.27 \pm 0.10‰$ (Savage et al., 2010) (Figure 2). The indistinguishable Si isotope composition of BHVO-2 processed through LC and traditional column chemistry indicates that the modified column procedure has not generated any artificial Si isotope fractionation. To further evaluate the effect of Fe-Ni-S matrices on Si isotope measurements, we doped purified NBS-28 solution with pure Ni and Fe (dissolved in 0.1 M HCl) to obtain Ni/Si and Fe/Si ratios of 0.1. The average $\delta^{30}Si$ of

this mixture was determined to be $0.00 \pm 0.03‰$ and $-0.08 \pm 0.04‰$, respectively. Considering the long-term $\delta^{30}Si$ reproducibility of $\pm 0.11‰$, the above results demonstrate that the matrix effect of Fe and Ni on Si isotope measurements using MC-ICPMS is negligible. To avoid complexities, Si isotope measurements were carried out only when the Fe/Si and Ni/Si of the purified samples were lower than 0.02.

One additional problem of Si isotope analyses in metallic fractions of EC is the high abundance of sulfides and phosphides associated with Si-bearing kamacite (Weisberg & Kimura, 2012). The cation exchange ion chromatography procedure does not effectively remove S and P from Si, and therefore, an overabundance of these anions in the samples might have an influence on the measured Si isotope composition (Chen et al., 2017; van den Boorn et al., 2009). The matrix effect of anions on mass spectrometric analyses of Si was tested at GFZ by doping purified NBS-28 solution with phosphate, sulfate, and nitrate anions to produce different [anion]/[Si] mass ratios ($\mu g\,\mu g^{-1}$) from 0.01 to 6.4 (Oelze et al., 2016). Oelze et al. (2016) reported that technical configurations such as external doping of Mg for Si isotope analyses and the use of Apex-Q desolvator along with Neptune Jet interface make the $\delta^{30}Si$ measurements less susceptible to matrix-induced bias caused by the presence of anionic impurities ($PO_4^{3-}$, $SO_4^{2-}$, and $NO_3^-$) at an uncertainty of $\pm 0.14‰$, 2SD. To avoid mass bias caused by the presence of anions in the samples, we have used the above-mentioned configuration and have not analyzed any samples with $[SO_4]/[Si]$ mass ratio outside the range tested by Oelze et al. (2016). Since the lightest Si isotope value of EC metal determined in this study (i.e., $\delta^{30}Si_{MSN} = -5.61 \pm 0.12‰$) is close to the published data on EC metals (Kadlag et al., 2019; Sikdar & Rai, 2020), we can suggest that our measurement protocol with combined standard-sample bracketing and Mg doping has not generated any matrix-induced bias on Si isotope data.

### Sample Preparation and Mass Spectrometry for Fe Isotope Analyses

The finely powdered samples weighing ~0.2–20 mg were digested in Savillex® PFA vials by sequential reflux and evaporation with a mixture of 4 mL concentrated HF–$HNO_3$ and 30% $H_2O_2$, 1 mL 6 M HCl, and concentrated $HNO_3$ at 120°C on a hot plate for several days. $HNO_3$–$H_2O_2$ was used to oxidize carbon species from the samples. Fe was fully oxidized to its trivalent state by repeated cycles of dissolution of all samples in concentrated $HNO_3$ followed by heating at 150°C and evaporating to dryness. Finally, all digested samples were dissolved in 1 mL 6 M HCl for chromatographic Fe separation. Iron in dissolved form was purified using 1 mL anion-exchange resin AG-1X8 (200–400 mesh) following procedures detailed elsewhere (Schoenberg & von Blanckenburg, 2005; Schuessler et al., 2016). The resin was pre-conditioned with 6 M HCl before sample loading, and matrix elements from the samples were removed using 6 M HCl. Fe was eluted from the sample solution with 4 mL MQ and 5 mL 5 M $HNO_3$. The Fe eluent was dried down and treated with 1 mL concentrated $HNO_3$ to decompose any resin particles removed from the columns. Samples were finally dissolved in 0.3 M $HNO_3$ for mass spectrometry. Aliquots of solutions before and after column chemistry were measured by ICP-OES to determine the recovery and purity of Fe after column chemistry. For certain samples, the entire procedure was repeated twice to ensure the removal of all matrix elements. The total procedural Fe blank from sample dissolution and column chromatography were determined to be <30 ng, which is negligible compared to the amount of Fe extracted from the samples, that is, ~30–80 µg.

For high precision Fe isotope analyses, samples were introduced into the mass spectrometer via $100\,\mu L\,min^{-1}$ PFA MicroFlow nebulizer and stable sample introduction system (SIS). MC-ICPMS was equipped with Nickel sampler and H skimmer cones, and the instrument was operated in medium resolution mode with a mass resolving power of 8200. Iron isotope measurements were performed on the flat top Fe peak shoulder to avoid polyatomic interferences from argide molecules on various isotopes of Fe. Instrumental mass bias was corrected using sample-standard bracketing with IRMM-014 as bracketing standard. Isotope analyses were acquired in a single block consisting of 25 cycles, and individual samples were measured two to four times to obtain the average $\delta^{56}Fe$ value reported in this study. The Fe concentrations of samples and standards ranged between 3 to 4 ppm at a sensitivity of $\sim 7\,V\,ppm^{-1}$ and acid background of <3 mV on $\delta^{56}Fe$. The same batch of 0.3 M $HNO_3$ was used for dilution of all solutions, including standards (IRMM-014) and blanks to ensure perfect matching in molarity and purity of sample and standard solutions. The Fe concentrations of sample and reference material (IRMM-014) were matched to within 5%. The mass spectrometric stability, repeatability, and accuracy of our Fe isotope analyses were evaluated during every analytical session by measuring Fe isotope composition of an in-house Fe standard at GFZ-Potsdam (HanFe standard, $\delta^{56}Fe = 0.301 \pm 0.046‰$). The Fe isotope composition of rock standards such as RGM-2 ($\delta^{56}Fe = 0.132 \pm 0.035‰$) and BR-1 ($\delta^{56}Fe = 0.122 \pm 0.013‰$) is in agreement with their published values of ~0.1‰ (Craddock & Dauphas, 2011; Poitrasson et al., 2004; Schoenberg & Blanckenburg, 2006), thereby demonstrating the robustness of our chemical and mass

spectrometric protocol. Based on repeat measurements of reference materials, the long-term reproducibility of Fe isotope analyses at GFZ was estimated to be ±0.05‰ (2SD) on $\delta^{56}$Fe.

## RESULTS

The Si and Fe isotope compositions of reference materials, bulk EC, and its physically separated components are reported in Tables 1 and 2, respectively. Analytical uncertainties associated with isotope measurements are given as 2 standard deviations (2SD) of the mean in the text. The Si isotope composition of different physically separated components of EC (Table 1) was found to be strongly heterogeneous, with the mean $\delta^{30}$Si ranging from $-5.61 \pm 0.12$‰ to $-3.28 \pm 0.05$‰ for MSNs; $-1.51 \pm 0.04$‰ to $-1.45 \pm 0.08$‰ for AMGs; $-1.03 \pm 0.08$‰ to $-0.66 \pm 0.05$‰ for magnetic fractions; $-0.48 \pm 0.17$‰ to $-0.32 \pm 0.08$‰ for SM fractions; $-0.48 \pm 0.05$‰ to $-0.32 \pm 0.06$‰ for NM fractions; and $0.05 \pm 0.12$‰ to $+0.23 \pm 0.10$‰ for the WMPs ($SiO_2$). Thus, the physically separated components of EC possess distinct $\delta^{30}$Si values, which are clearly resolvable within the uncertainty of our analytical precision. The $\delta^{30}$Si values of the BM fractions of EC ($-0.74 \pm 0.10$‰ to $-0.59 \pm 0.12$‰) lie between their magnetic and NM phase separates.

The mean $\delta^{56}$Fe of different EC components was found to range from $+0.089 \pm 0.032$‰ to $+0.196 \pm 0.038$‰ for MSNs, $+0.072 \pm 0.035$‰ to $+0.114 \pm 0.042$‰ for AMGs, $-0.023 \pm 0.053$‰ to $+0.140 \pm 0.046$‰ for magnetic fractions, $-0.041 \pm 0.041$‰ to $+0.042 \pm 0.009$‰ for SM fractions, and $-0.305 \pm 0.077$‰ to $+0.032 \pm 0.020$‰ for the NM fractions (Table 2). On average, the $\delta^{56}$Fe values of MSNs were slightly heavier than the AMGs and matrix-bound magnetic fractions (i.e., matrix metals), which were in turn heavier compared to their SM and NM counterparts. Overall, the magnetic fractions of EC have systematically heavier $\delta^{56}$Fe by at least ~0.1‰ compared to the corresponding NM (sulfides+silicates) fractions. The $\delta^{56}$Fe values of the BM fractions of the studied EC range from $0.001 \pm 0.060$‰ to $0.058 \pm 0.023$‰.

It is emphasized that physical separation of chondritic components is not always perfect as fine metals often adhere to non-metals (silicates and sulfides) and vice versa. Since the abundance of isotopically distinct magnetic and NM phases can be significantly variable in the sampled chondritic components, incomplete separation of metals from silicates or sulfides and vice versa can dramatically influence the isotope composition of the separated chondrite fractions, thereby leading to sampling bias. Therefore, the data reported here may not represent the true endmembers of Si and Fe isotope heterogeneity in EC, which is expected to be more extreme, at least on the metallic side of $\delta^{30}$Si and on the sulfidic side of $\delta^{56}$Fe. It is noted that Si isotope analyses could not be performed for some samples such as MF and SM fractions of Kota-Kota and NM fraction of Indarch, etc. (Table 1). Similarly, the SM fraction of Indarch and the NM fraction of Abee could not be measured for their Fe isotope composition (Table 2). This was either because of low Si or Fe concentrations in their sample solution or the chromatographically purified samples did not pass the requisite purity and yield test.

## DISCUSSION

Despite the significant variations of Si and Fe isotope composition in different physically separated components of EC, all data points follow single mass-dependent fractionation lines on three-isotope diagrams of $\delta^{29}$Si versus $\delta^{30}$Si (Figure 3) and $\delta^{56}$Fe versus $\delta^{57}$Fe (Figure 4), respectively. The lack of any resolvable deviation from mass fractionation lines indicate that the EC components have undergone mass-dependent Si and Fe isotope fractionation, and any nucleosynthetic anomalies inherited by the EC parent bodies from different stellar sources are below our analytical uncertainties. Chondrites are cosmic agglomerates of diverse materials and the heterogeneous composition of its different components was established through repeated heating, evaporation, and condensation cycles during proto-planetary disk evolution, which may have been modified later by processes on their parent bodies (Scott & Krot, 2007, 2014). Here, we first evaluate the origin of the observed mass-dependent Si and Fe isotope fractionations among diverse EC components (see "Origin of Si and Fe Isotope Heterogeneity in EC" Section). Subsequently, we discuss the implications of the observed isotope fractionations on gas–solid interaction processes in the nebula (see "Gas–Solid Interaction Processes in Reduced Nebular Environment" Section), lateral mixing between inner and outer solar system bodies (see "Homogeneous $\delta^{56}$Fe of the Solar System" Section), and on the mass-dependent Si and Fe isotope composition of the Earth (see "Implications for Si and Fe Isotope Composition of the Earth" Section).

### Origin of Si and Fe Isotope Heterogeneity in enstatite chondrites

The potential pathways to generate Si and Fe isotope fractionation in chondritic components include terrestrial weathering, diverse parent body processes (aqueous alteration, impact melting, thermal metamorphism), and nebular scale processes (gas–solid interactions in the nebula and/or changes in redox conditions of the

TABLE 1. Si isotope composition of reference materials, bulk enstatite chondrites, and their physically separated components.

| Meteorite name/sample ID | Range of $\delta^{30}$Si (‰) ± 2SE | Average $\delta^{30}$Si (‰) ± 2SE | 2SD | Mg# | *N* |
|---|---|---|---|---|---|
| **Reference materials** | | | | | |
| Diatomite | +1.08 (±0.08) to +1.27 (±0.09) | 1.13 (0.04) | 0.12 | – | 9 |
| Big Batch | −10.75 (±0.08) to −10.62 (±0.08) | −10.67 (0.08) | 0.14 | – | 3 |
| RGM-2 | −0.35 (±0.12) to −0.33 (±0.08) | −0.34 (0.02) | 0.03 | – | 2 |
| BHVO-2 (traditional col-I) | −0.35 (±0.08) to −0.19 (±0.08) | −0.27 (0.04) | 0.11 | – | 6 |
| BHVO-2 (traditional col-II) | −0.39 (±0.13) to −0.30 (±0.09) | −0.34 (0.03) | 0.08 | – | 7 |
| BHVO-2 (long column) | −0.41 (±0.08) to −0.25 (±0.09) | −0.31 (0.05) | 0.12 | – | 6 |
| **Bulk meteorites** | | | | | |
| Sahara 97072 (EH3) | −0.59 (±0.08) | −0.59 (0.08) | 0.12[a] | 0.23 | 1 |
| MAC 88184 (EL3) | −0.72 (±0.07) to −0.67 (±0.08) | −0.70 (0.04) | 0.06 | 0.15 | 2 |
| Abee (EH4) | −0.74 (±0.08) to −0.70 (±0.09) | −0.72 (0.03) | 0.04 | 0.12 | 3 |
| Indarch (EH4) | −0.80 (±0.11) to −0.70 (±0.11) | −0.74 (0.06) | 0.10 | 0.26 | 3 |
| **Metal–sulfide nodules** | | | | | |
| Kota-Kota Nod 1 (>250 μm) | −5.36 (±0.09) to −5.27 (±0.08) | −5.31 (0.09) | 0.12 | 0.012 | 2 |
| Nod 2 (>250 μm) | −5.01 (±0.08) to −4.98 (±0.09) | −5.00 (0.03) | 0.04 | 0.011 | 2 |
| Nod 3 (>250 μm) | −5.61 (±0.08) | −5.61 (0.08) | 0.12[a] | 0.006 | 1 |
| Sahara 97072 Nod 1 (<250 μm) | −3.31 (±0.09) to −3.25 (±0.08) | −3.28 (0.03) | 0.05 | 0.024 | 4 |
| Nod 2 (<250 μm) | −3.39 (±0.12) to −3.17 (±0.08) | −3.28 (0.09) | 0.18 | 0.025 | 4 |
| Nod 3 (>250 μm) | −5.13 (±0.13) | −5.13 (0.13) | 0.12[a] | 0.006 | 1 |
| **Angular metal grains (AMGs)** | | | | | |
| Kota-Kota | −1.54 (±0.07) to −1.48 (±0.07) | −1.51 (0.02) | 0.04 | 0.023 | 4 |
| Sahara 97072 AMG #1 | −1.51 (±0.10) to −1.49 (±0.07) | −1.50 (0.02) | 0.03 | 0.061 | 2 |
| AMG #2 | −1.50 (±0.08) to −1.43 (±0.08) | −1.45 (0.05) | 0.08 | 0.098 | 3 |
| **Magnetic fractions** | | | | | |
| Sahara 97072 | −1.08 (±0.09) to −1.01 (±0.08) | −1.03 (0.04) | 0.08 | 0.143 | 3 |
| MAC 88184 | −0.69 (±0.09) to −0.64 (±0.09) | −0.66 (0.03) | 0.05 | 0.281 | 3 |
| Indarch | −0.99 (±0.10) to −0.96 (±0.09) | −0.98 (0.03) | 0.04 | 0.216 | 2 |
| **Slightly magnetic fractions** | | | | | |
| Sahara 97072 | −0.35 (±0.06) to −0.29 (±0.09) | −0.32 (0.06) | 0.08 | 0.615 | 2 |
| Abee | −0.38 (±0.10) | −0.38 (0.10) | 0.12[a] | 0.503 | 1 |
| Indarch | −0.54 (±0.09) to −0.42 (±0.11) | −0.48 (0.12) | 0.17 | 0.757 | 2 |
| **Non-magnetic fractions** | | | | | |
| Kota-Kota | −0.34 (±0.07) to −0.29 (±0.09) | −0.32 (0.03) | 0.06 | 0.748 | 3 |
| Sahara 97072 NM #1 | −0.46 (±0.08) to −0.43 (±0.09) | −0.45 (0.03) | 0.04 | 0.738 | 2 |
| NM #2 | −0.48 (±0.07) to −0.34 (±0.07) | −0.41 (0.13) | 0.19 | 0.750 | 2 |
| NM #3 | −0.36 (±0.07) to −0.32 (±0.08) | −0.34 (0.02) | 0.04 | 0.825 | 3 |
| MAC 88184 | −0.50 (±0.09) to −0.45 (±0.07) | −0.48 (0.03) | 0.05 | 0.563 | 3 |
| Abee | −0.32 (±0.08) | −0.32 (0.08) | 0.12[a] | 0.592 | 1 |
| **White mineral phases ($SiO_2$)** | | | | | |
| Kota-Kota | 0.05 (±0.09) | 0.05 (0.09) | 0.12[a] | 0.821 | 1 |
| Sahara 97072 | +0.18 (±0.11) to +0.27 (±0.09) | 0.23 (0.06) | 0.10 | 0.924 | 3 |
| **NWA 5492 (UNG chondrite)** | | | | | |
| Bulk meteorite #1 | −0.45 (±0.09) to −0.43 (±0.08) | −0.44 (0.02) | 0.03 | – | 2 |
| #2 | −0.42 (±0.08) to −0.34 (±0.09) | −0.39 (0.05) | 0.09 | – | 3 |
| **Average (bulk NWA 5492)** | | **−0.42** (0.05) | **0.07** | – | **2*** |
| Non-magnetic fraction #1 | −0.47 (±0.09) to −0.39 (±0.08) | −0.44 (0.05) | 0.09 | – | 3 |
| #2 | −0.50 (±0.10) to −0.46 (±0.08) | −0.48 (0.03) | 0.05 | – | 2 |
| Average (NM NWA 5492) | | **−0.46** (0.04) | **0.06** | – | **2*** |

*Note*: The Si isotope composition of non-magnetic and bulk meteorite fractions of an ungrouped chondrite NWA 5492 is also provided. Mg# = molar $Mg/(Mg+Fe^{2+})$. The bold values represent average values of BM and NM fraction of NWA 5492.

[a]In case of single measurement, that is, $n = 1$, uncertainty has been estimated based on repeat measurements of reference material BHVO-2. *N* refers to the number of repeat analyses of the same digestion aliquot of a sample. For average values, *N** has been provided, which refers to the total number of samples representative of each category. Since metals often adhere to non-metals (silicates and sulfides) and vice versa, the data provided here may not represent the true end-members of Si isotope heterogeneity among EC components.

TABLE 2. Fe isotope composition and elemental ratios [i.e., Mg# = molar Mg/(Mg+$Fe^{2+}$) and Ni/S] of reference materials, bulk enstatite chondrites, and their physically separated components.

| Meteorite name/sample ID | Range of $\delta^{56}$Fe (‰) ± 2SE | Average $\delta^{56}$Fe(‰) ± 2SE | 2SD | Mg# | Ni/S | *N* |
|---|---|---|---|---|---|---|
| **Reference materials** | | | | | | |
| HanFe | +0.258 (±0.023) to +0.348 (±0.040) | 0.301 (0.001) | 0.046 | – | – | 21 |
| RGM-2 | +0.115 (±0.051) to +0.156 (±0.052) | 0.132 (0.002) | 0.035 | – | – | 4 |
| BR-1 | +0.117 (±0.044) to +0.131 (±0.041) | 0.122 (0.001) | 0.013 | – | – | 4 |
| **Bulk meteorite fractions** | | | | | | |
| Kota-Kota (EH3) | +0.024 (±0.028) to +0.063 (±0.033) | 0.040 (0.016) | 0.033 | 0.23 | 0.43 | 4 |
| Sahara 97072 (EH3) | +0.022 (±0.025) to +0.036 (±0.024) | 0.030 (0.001) | 0.015 | 0.22 | 0.45 | 3 |
| MAC 88184 (EL3) | −0.024 (±0.055) to +0.041 (±0.041) | 0.001 (0.029) | 0.060 | 0.48 | 0.16 | 4 |
| Abee (EH4) | +0.020 (±0.038) | 0.020 (0.038) | 0.046[a] | 0.53 | 0.03 | 1 |
| Indarch (EH4) | +0.050 (±0.022) to +0.066 (±0.025) | 0.058 (0.016) | 0.023 | 0.25 | 0.32 | 2 |
| **Metal–sulfide nodules** | | | | | | |
| Kota-Kota Nod 1 (>250 μm) | +0.123 (±0.017) to +0.142 (±0.023) | 0.131 (0.011) | 0.020 | 0.01 | 1.53 | 3 |
| Nod 2 (<250 μm) | +0.071 (±0.025) to +0.139 (±0.028) | 0.115 (0.030) | 0.061 | 0.01 | 1.33 | 4 |
| Sahara 97072 Nod 1 (<250 μm) | +0.071 (±0.023) to +0.107 (±0.027) | 0.089 (0.015) | 0.032 | 0.02 | 0.85 | 4 |
| Nod 2 (>250 μm) | +0.177 (±0.020) to +0.222 (±0.024) | 0.196 (0.018) | 0.038 | 0.02 | 1.44 | 4 |
| **Angular metal grains** | | | | | | |
| Kota-Kota | +0.047 (±0.025) to +0.084 (±0.025) | 0.072 (0.017) | 0.035 | 0.02 | 0.95 | 4 |
| Sahara 97072 | +0.091 (±0.023) to +0.136 (±0.019) | 0.114 (0.021) | 0.042 | 0.06 | 0.53 | 4 |
| **Magnetic fractions** | | | | | | |
| Kota-Kota | +0.123 (±0.056) to +0.136 (±0.049) | 0.129 (0.012) | 0.018 | – | – | 2 |
| Sahara 97072 | +0.119 (±0.044) to +0.142 (±0.060) | 0.130 (0.022) | 0.032 | 0.13 | 0.85 | 2 |
| MAC 88184 | −0.045 (±0.046) to +0.006 (±0.050) | −0.023 (0.030) | 0.053 | 0.28 | 0.61 | 3 |
| Abee | +0.017 (±0.020) to +0.042 (±0.019) | 0.032 (0.014) | 0.026 | 0.14 | 1.01 | 3 |
| Indarch | +0.121 (±0.049) to +0.172 (±0.050) | 0.140 (0.022) | 0.046 | 0.13 | 0.59 | 4 |
| **Slightly magnetic fractions** | | | | | | |
| Kota-Kota | +0.039 (±0.024) to +0.046 (±0.024) | 0.042 (0.007) | 0.009 | 0.37 | 0.11 | 2 |
| Sahara 97072 | −0.065 (±0.020) to −0.027 (±0.025) | −0.041 (0.023) | 0.041 | 0.61 | 0.07 | 3 |
| MAC 88184 | −0.027 (±0.023) | −0.027 (0.023) | 0.046[a] | 0.33 | 0.56 | 1 |
| Abee | −0.006 (±0.020) to +0.019 (±0.027) | 0.007 (0.025) | 0.036 | 0.50 | 0.03 | 2 |
| **Non-magnetic fractions** | | | | | | |
| Kota-Kota | +0.018 (±0.019) to +0.041 (±0.019) | 0.032 (0.001) | 0.020 | 0.81 | 0.02 | 4 |
| Sahara 97072 | −0.054 (±0.022) to −0.049 (±0.024) | −0.052 (0.006) | 0.018 | 0.74 | 0.08 | 4 |
| MAC 88184 | −0.272 (±0.048) to −0.355 (±0.048) | −0.305 (0.038) | 0.077 | 0.88 | 0.05 | 4 |
| Indarch | −0.213 (±0.050) to −0.292 (±0.051) | −0.255 (0.045) | 0.080 | 0.78 | 0.003 | 4 |
| **NWA 5492 (UNG chondrite)** | | | | | | |
| Bulk meteorite | +0.042 (±0.020) | 0.042 (0.020) | 0.046[a] | 0.12 | 6.02 | 4 |
| Magnetic fraction | +0.168 (±0.040) to +0.247 (±0.043) | 0.206 (0.032) | 0.065 | 0.02 | 13.9 | 4 |
| Non-magnetic fraction #1 | −0.107 (±0.023) to −0.160 (±0.021) | −0.128 (0.023) | 0.048 | – | – | 4 |
| #2 | −0.122 (±0.022) to −0.149 (±0.023) | −0.134 (0.011) | 0.023 | – | – | 4 |
| Average NM fraction | | −0.131 | 0.008 | – | – | |
| **Ordinary chondrites** | | | | | | |
| WSG 95300 (H3) | | | | | | |
| Magnetic fraction | +0.148 (±0.053) to +0.242 (±0.047) | 0.198 (0.054) | 0.095 | 0.15 | 4.29 | 3 |
| Non-magnetic fraction #1 | −0.190 (±0.046) to −0.273 (±0.054) | −0.233 (0.036) | 0.072 | 0.56 | 0.04 | 4 |
| #2 | −0.113 (±0.045) to −0.195 (±0.056) | −0.158 (0.033) | 0.068 | 0.59 | 0.02 | 4 |
| #3 | −0.181 (±0.045) to −0.61 (±0.045) | −0.170 (0.011) | 0.020 | 0.43 | – | 3 |
| QUE 97008 (LL 3.05) | | | | | | |
| Magnetic fraction | +0.265 (±0.043) to +0.308 (±0.043) | 0.286 (0.043) | 0.062 | 0.18 | – | 2 |

*Note*: Fe isotope composition of magnetic and non-magnetic phase separates of an ungrouped chondrite and two ordinary chondrites is also provided.

[a]In case of single measurement, that is, $n = 1$, the uncertainty has been estimated based on repeat measurements of reference material HanFe. *N* refers to the number of repeat analyses of the same digestion aliquot of a sample. Note that the data provided here may not represent the true end-member Fe isotope composition of metal and sulfide fractions of EC due to the possibility of sampling bias during physical separation of chondrite components.

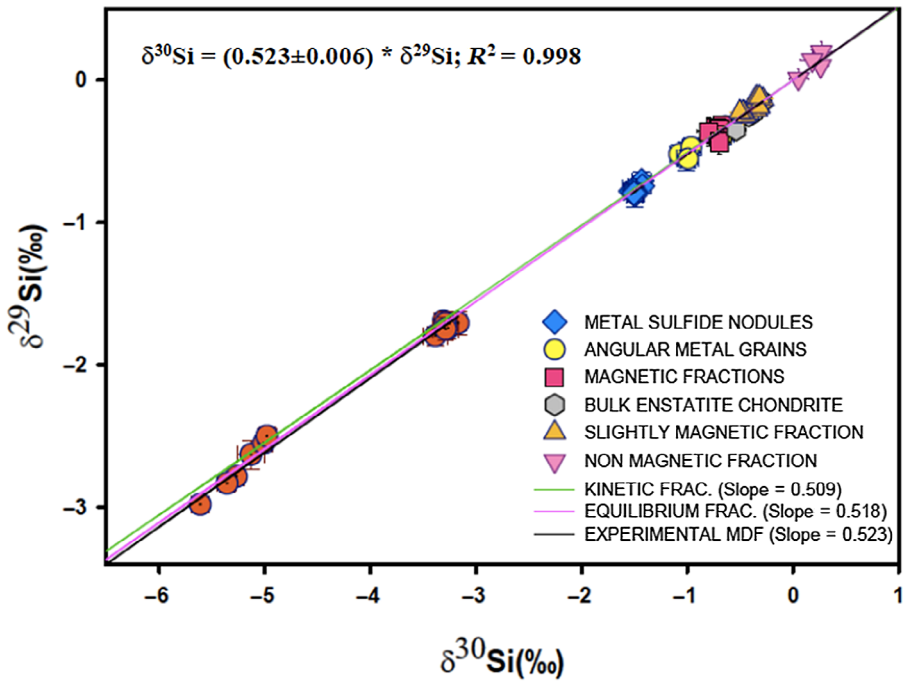


FIGURE 3. In a $\delta^{29}Si$ versus $\delta^{30}Si$ plot, all components of enstatite chondrites analyzed in this study lie on a mass-dependent fractionation line with a best-fit slope of $0.523 \pm 0.006$, 2 SE. The error bars represent 2SD of the mean. The calculated slopes for mass-dependent equilibrium (0.518) and kinetic fractionation (0.509) are also plotted. (Color figure can be viewed at wileyonlinelibrary.com)

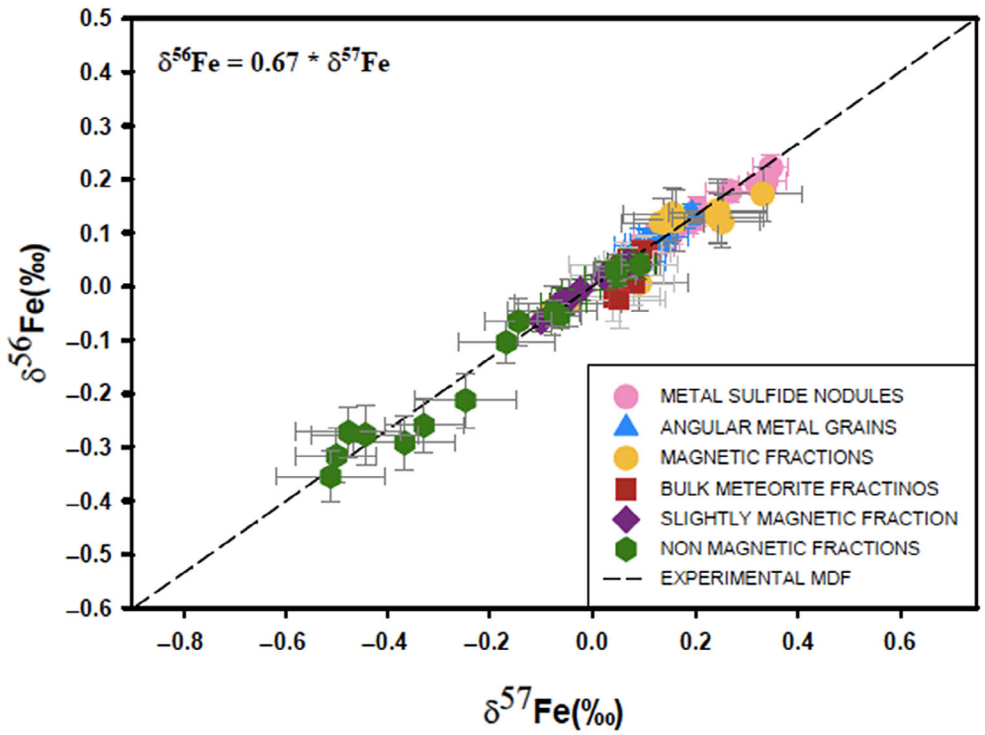


FIGURE 4. $\delta^{56}Fe$ versus $\delta^{57}Fe$ plot shows that all components of the studied enstatite chondrites lie on a mass-dependent fractionation line with best-fit slope of 0.67. The error bars represent 2SD of the mean. (Color figure can be viewed at wileyonlinelibrary.com)

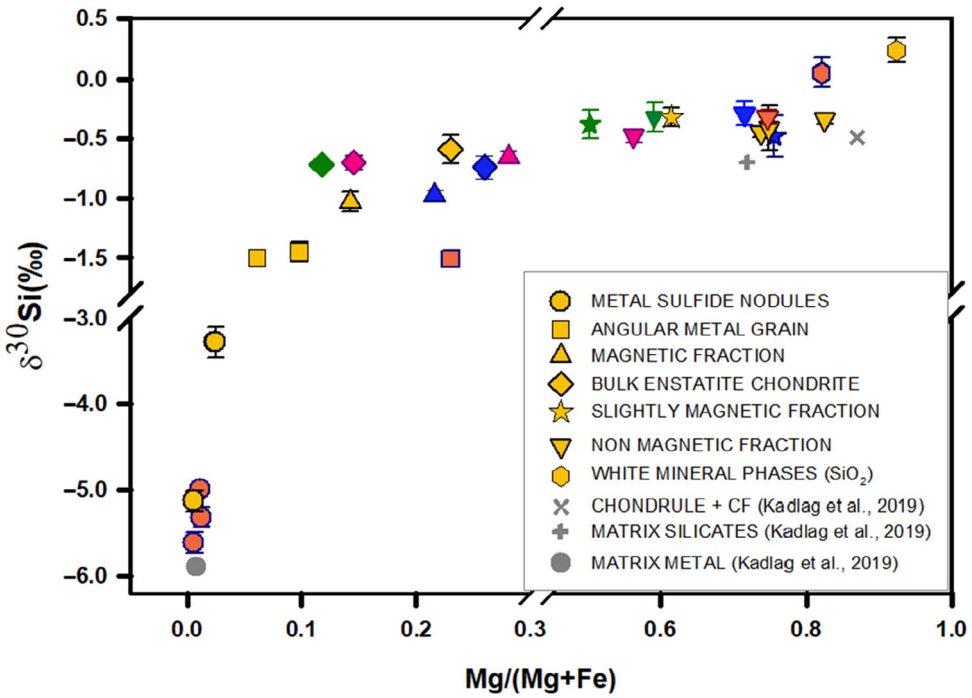


FIGURE 5. Plot of $\delta^{30}$Si versus Mg# (=Mg/(Mg+Fe)) in different components of enstatite chondrites shows that $\delta^{30}$Si becomes progressively heavier with decreasing metal content. The color codes used are as follows, Yellow: Sahara 97072, Red: Kota-Kota, Pink: MAC 88184, Green: Abee, and Blue: Indarch. Gray-colored symbols indicate literature data. (Color figure can be viewed at wileyonlinelibrary.com)

chondrite forming region). These pathways are discussed in detail in the following subsections.

### *Terrestrial Weathering and Aqueous Alteration*

Among the five ECs analyzed in this study, Sahara 97072, Kota-Kota, and MAC 88184 are finds with low degrees of weathering, whereas Abee and Indarch are observed falls. The average $\delta^{30}$Si of the finds (i.e., Sahara 97072, Kota-Kota, and MAC 88184) and falls (i.e., Abee and Indarch) are $-0.64 \pm 0.15‰$ and $-0.73 \pm 0.03‰$, respectively. The average $\delta^{56}$Fe of the studied finds and falls are $0.023 \pm 0.040‰$ and $0.039 \pm 0.053‰$, respectively. Thus, there are no obvious difference in the $\delta^{30}$Si and $\delta^{56}$Fe values between falls versus finds, which suggests that the Si and Fe isotope compositions of the studied chondrites were not significantly affected by terrestrial weathering. In general, terrestrial weathering and formation of fusion crusts on meteorites are known to enrich meteorites in heavy Fe isotopes by up to 0.1‰ (Hezel et al., 2015; Saunier et al., 2010). This is significantly smaller compared to the total range of $\delta^{56}$Fe measured in EC components (i.e., ~0.4‰), which indicates that terrestrial weathering cannot explain the observed isotope fractionation. Furthermore, the chondritic components were carefully sampled only from their fresh interior portions to make sure the studied phases are free from fusion crusts, alteration products, and terrestrial contamination. Additionally, the ECs analyzed here do not display any evidence of aqueous alteration or clay formation in their fine-grained matrices. Given this, we can suggest that the stable Si and Fe isotope variations in EC components most likely record processes that occurred at higher temperatures, either in the nebula and/or on the EC parent bodies.

### *Metal–Silicate–Sulfide Partitioning at Low Oxygen Fugacity*

The geochemical affinities of Si and Fe to get partitioned among metal–silicate–sulfidic phases can significantly fractionate Si and Fe isotope composition. The major host phases of Si in EC are the silicate minerals (i.e., enstatite, forsterite, silica, plagioclase) and Si-bearing Fe-Ni metal. The studied EC components display a positive correlation between $\delta^{30}$Si and Mg number (Mg# = molar Mg/(Mg+Fe)), Figure 5, which indicates that $\delta^{30}$Si becomes progressively heavier from metal-rich components (i.e., MSN, AMG, matrix-bound magnetic fractions, and SM fractions) towards the silicate-rich components (i.e., the NM fractions and WMPs). This observation illustrates a key role of metal–silicate partitioning in fractionating Si isotopes in EC-like reduced planetary bodies. Our results are consistent with previous Si isotope data in EC phase separates (Kadlag et al., 2019; Sikdar & Rai, 2020; Ziegler et al., 2010),

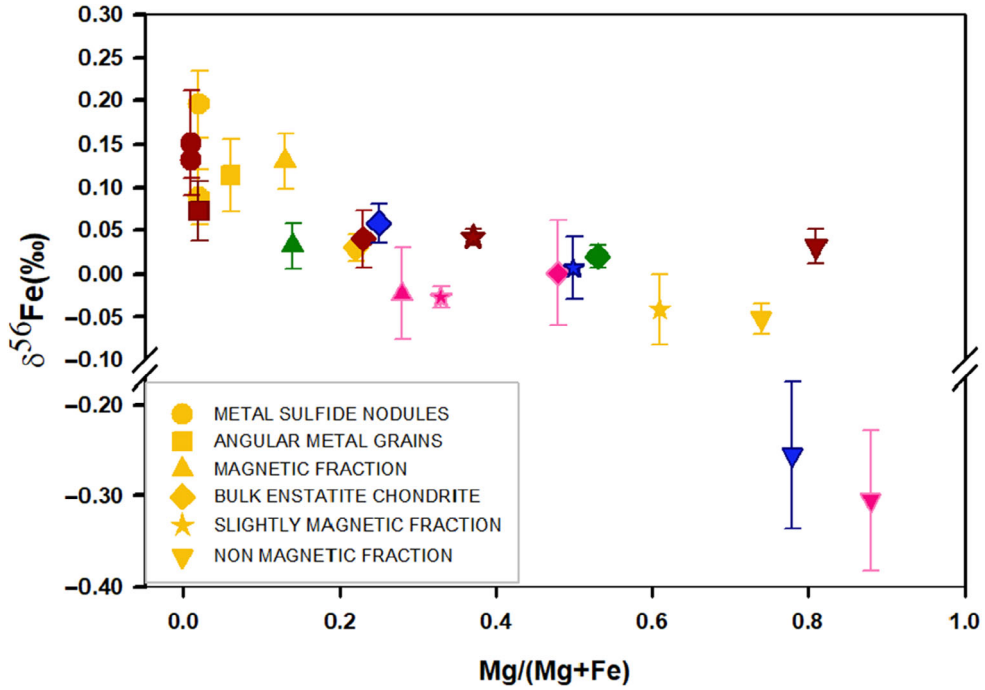


FIGURE 6. Negative correlation between $\delta^{56}$Fe and Mg# in EC components indicates that Fe isotope fractionation was governed by the partitioning of Fe between metal and non-metallic fractions of enstatite chondrites. The color codes used are as follows, Yellow: Sahara 97072, Red: Kota-Kota, Pink: MAC 88184, Green: Abee, and Blue: Indarch. The larger uncertainty associated with NM fraction of Indarch and MAC 88184 could be due to low Fe content in these samples. These two samples were still measured because they passed the requisite yield and purity test. (Color figure can be viewed at wileyonlinelibrary.com)

results from high temperature–pressure experiments (Shahar et al., 2011), and ab initio calculations (Javoy et al., 2012), which have demonstrated that reduced metals are enriched in light Si isotopes compared to the corresponding silicate fractions.

The variable $\delta^{30}$Si of metal- and silicate-rich fractions could be related to incomplete separation of the fine-grained metallic and silicate endmembers during their physical separation process and/or could be inherited from isotopically variable precursor materials. We found that the $\delta^{30}$Si values of MSNs vary according to the respective size fractions of the individual nodules, that is, the coarser MSNs of Sahara 97072 (size >250 μm) possess lighter Si isotope composition (average $\delta^{30}$Si $= -5.13 \pm 0.12$‰, $n = 1$) compared to the smaller nodules (<250 μm, average $\delta^{30}\text{Si} = -3.28 \pm 0.00$‰, $n = 2$). With decrease in the size of metal grains, the possibility of sampling pure metallic end-members (while avoiding dilution from surrounding silicates) also decreases. Therefore, the smaller nodules tend to have a higher proportion of isotopically heavier silicates attached to them, which could be a possible explanation for the heavier $\delta^{30}$Si of smaller MSNs compared to that of the larger nodules. Thus, mixing of different proportions of isotopically distinct metals and silicates can provide a viable explanation of the observed $\delta^{30}$Si variations among EC components.

We also observed a negative correlation between $\delta^{56}$Fe and Mg# in the EC components (Figure 6), which suggests that Fe isotope fractionation is mostly associated with the partitioning of Fe between metals in the magnetic fractions and silicates/sulfides in the NM fractions. In the NM fractions of EC, Fe is hosted predominantly by troilite (FeS), whereas the silicate phases contain only a minor fraction of Fe (Kallemeyn & Wasson, 1986). For example, on average, the metal and sulfide phases contain approximately 49.5 and 49.4 wt% of all Fe in EC, whereas the silicate phases account for only 1.06 wt% of total Fe in EC (Wang et al., 2014). Because the abundance of Fe in EC silicates is minor, mass balance suggests that the silicates should not have a significant contribution on the $\delta^{56}$Fe values of EC. In this study, we have used the Ni/S ratio (determined using ICP-OES in the same digestion aliquot used for Fe isotope analyses) to provide a measure of the relative contributions of metal and sulfides in the studied samples. Nickel has been considered instead of Fe because Ni exhibits the most siderophile character among all major elements, and therefore, Ni has lesser tendency to partition into sulfides compared to Fe (Chabot et al., 2017). Additionally, the Ni content in troilite grains of EH

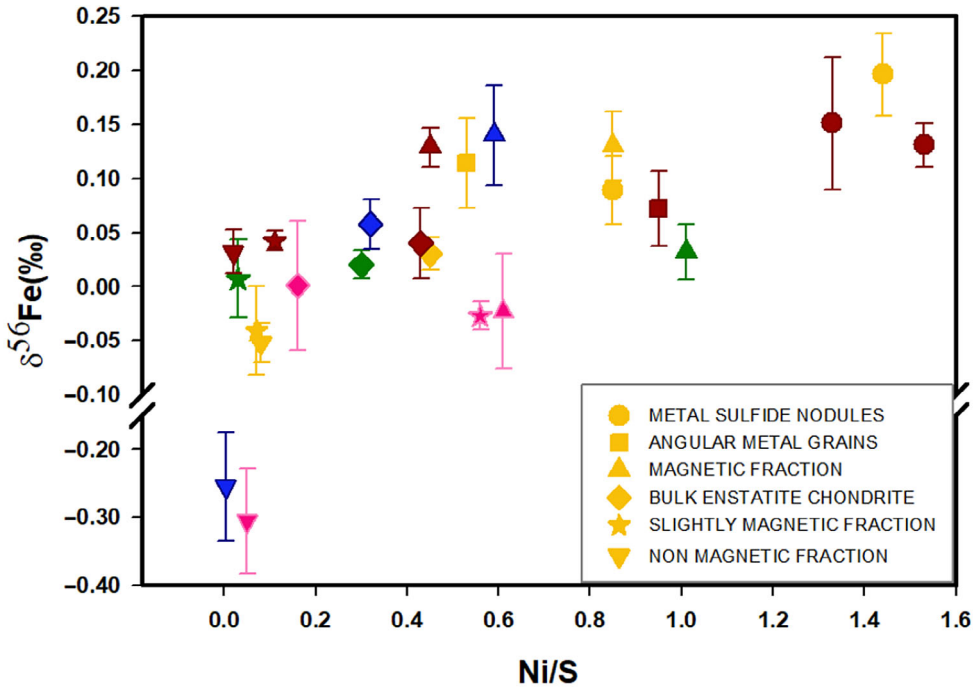


FIGURE 7. Correlated variation between $\delta^{56}$Fe and Ni/S in EC components demonstrates that Fe isotopes in EC were predominantly affected by metal–sulfide fractionation. The color codes used are as follows, Yellow: Sahara 97072, Red: Kota-Kota, Pink: MAC 88184, Green: Abee, and Blue: Indarch. (Color figure can be viewed at wileyonlinelibrary.com)

and EL chondrites is negligible, ranging from $0.07 \pm 0.01$ to $0.11 \pm 0.02$ wt% (Lin & Kimura, 1998; Patzer et al., 2004). Because of the low abundance of Ni in troilite, the Ni/S ratio of the physically separated fractions of EC is strongly affected by its metal–sulfide mass ratio. Our observation that the $\delta^{56}$Fe of EC components become progressively heavier with increasing Ni/S ratio (Figure 7) suggests that sulfides are the main host of light Fe isotopes in the NM fractions of EC. This observation agrees well with theoretical predictions and experimental studies, which have demonstrated that troilites are enriched in lighter Fe isotopes compared to the co-existing magnetic phases at 1000°C or below (Schauble et al., 2001; Schuessler et al., 2007; Williams et al., 2006). Thus, the distinct $\delta^{56}$Fe values of diverse physically separated components of EC, coupled with the negative correlation between $\delta^{56}$Fe and Mg# (Figure 6) and positive correlation between $\delta^{56}$Fe and Ni/S (Figure 7), reflect that the observed Fe isotope fractionation is mostly associated with the partitioning of Fe among metal and sulfidic phases of EC, and not with metal–silicate Fe isotope partitioning.

Upon combining both Si and Fe isotope data, we observed an inverse correlation between $\delta^{30}$Si and $\delta^{56}$Fe among the different physically separated fractions of EC (Figure 8). For example, the coarser MSNs of Sahara 97072, with the lightest $\delta^{30}$Si composition ($-5.61 \pm 0.12$‰) possess the heaviest $\delta^{56}$Fe ($+0.196 \pm 0.038$‰). On the other hand, its NM fractions possess relatively heavier Si (average $\delta^{30}Si_{EC\_NM} = -0.40 \pm 0.11$‰, $n = 3$) and lighter Fe isotope composition ($\delta^{56}Fe_{EC\_NM} = -0.052 \pm 0.018$‰). This trend of lighter $\delta^{30}$Si and heavier $\delta^{56}$Fe in the magnetic fractions compared to that in their NM counterparts was also observed in the component separates of Kota-Kota (EH3), Abee (EH4), Indarch (EH4), and MAC 88184 (EL3). The $\delta^{30}$Si and $\delta^{56}$Fe values of AMGs, magnetic fractions, and BM fractions vary between MSNs and NM fractions depending on the relative proportions of Si and Fe content in the separated mineral mixtures. Comparing the results of high-temperature isotope exchange experiments by Hin et al. (2014) and Shahar et al. (2015) reflects that the directions of metal–silicate equilibrium isotope fractionation factors of silicon and iron are opposite of each other, which is consistent with the inverse correlation between $\delta^{30}$Si and $\delta^{56}$Fe observed in diverse EC components. Thus, metal–silicate Si isotope partitioning and metal–sulfide Fe isotope partitioning at low oxygen fugacity provide a first-order explanation of the anti-correlated Si and Fe isotope variations observed in EC components (Figure 8). However, the formation conditions (temperature, pressure, oxygen fugacity, etc.) of EC were significantly different than the experimental conditions, and given the differences in the magnitude of

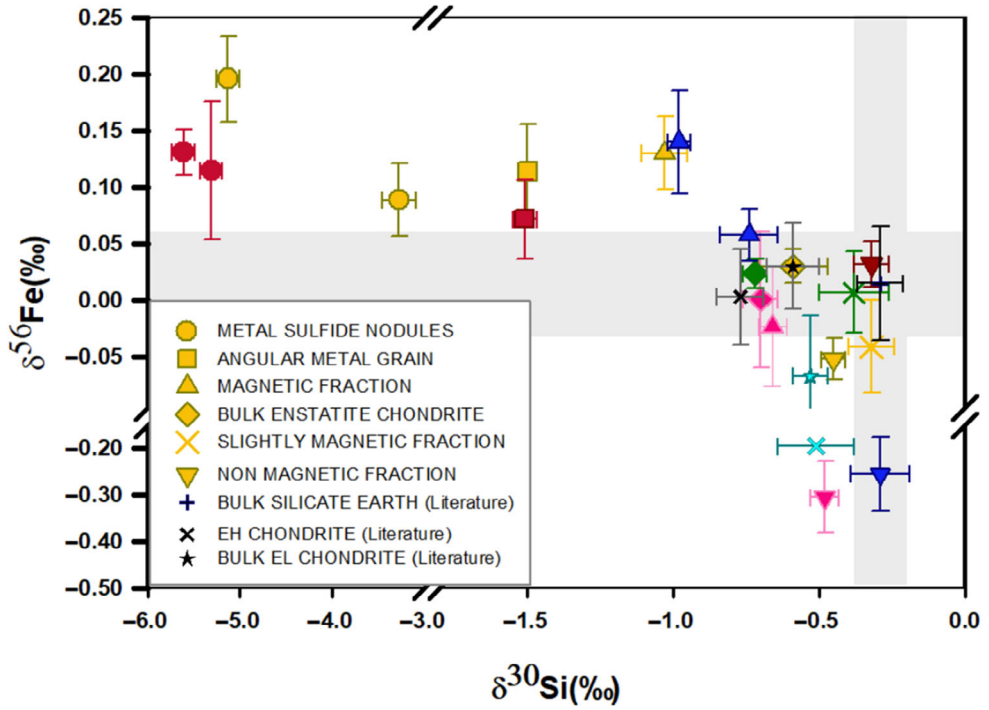


FIGURE 8. Inverse correlation between $\delta^{30}$Si and $\delta^{56}$Fe among different components of EC, that is, $\delta^{30}$Si becomes heavier from magnetic to non-magnetic fractions whereas $\delta^{56}$Fe becomes progressively lighter. The color codes used are as follows, Yellow: Sahara 97072, Red: Kota-Kota, Pink: MAC 88184, Green: Abee, and Blue: Indarch. Gray-colored symbols refer to literature data. The horizontal and vertical bars represent the range of Si and Fe isotope variations in BSE, which has an average $\delta^{30}$Si of $-0.29 \pm 0.08$‰ (Savage et al., 2010) and $\delta^{56}$Fe of $+0.015 \pm 0.018$‰ (Weyer et al., 2005). (Color figure can be viewed at wileyonlinelibrary.com)

Si and Fe isotope fractionation between experimental results and EC data, it is unlikely that mixing of isotopically distinct phases in variable proportions alone can explain the observed isotope fractionation. Instead, the Si and Fe isotope distributions in EC must have contributions from isotopically variable precursor materials or they were affected by different parent body processes or both.

### *Nebular Origin of the lighter $\delta^{30}$Si of Bulk enstatite chondrites*

The Si isotope compositions of bulk EC (average $\delta^{30}Si_{BM} = -0.69 \pm 0.14$‰, this study) plot between its metal-rich and silicate-rich endmembers (Figure 5). The most straightforward interpretation of this observation is that the lighter $\delta^{30}$Si of bulk EC compared to OC and CC (average $\delta^{30}Si_{CC\text{-}OC} = -0.46 \pm 0.02$‰, 2SE, Zambardi et al., 2013) is governed by the significantly lighter Si isotopic composition of EC metals (Kadlag et al., 2019; Savage & Moynier, 2013; Sikdar & Rai, 2020, this study). However, the average abundance of Si in EC metals is significantly lower (~3 wt% Si, Ringwood, 1960) compared to that in silicates (~97 wt%). Hence, mass balance requires that Si isotope composition of the silicate phases has an important control on the Si isotope composition of bulk EC. To evaluate the degree of Si isotope homogeneity in EC silicates, three different aliquots of NM fractions from Sahara 97072 were processed and analyzed separately. Within the limits of our analytical uncertainties, it is evident that the different NM fractions of Sahara 97072 are not homogeneous, with $\delta^{30}$Si varying from $-0.45 \pm 0.04$‰ to $-0.34 \pm 0.04$‰. The $\delta^{30}$Si values of the NM fractions of Kota-Kota, Abee, and MAC 88184 ranged from $-0.48 \pm 0.05$‰ to $-0.32 \pm 0.06$‰, indicating that the silicates of EC can have $\delta^{30}$Si values similar to bulk OC-CC and/or heavier. Additionally, we found that the WMPs, which are also silicates composed predominantly of $SiO_2$, possess the heaviest $\delta^{30}$Si among all studied components. Since the $\delta^{30}$Si values of the NM fractions of EC are largely independent of the metal content and Mg/Fe ratio, we suggest that the incorporation of light Si in EC metals alone cannot explain the overall lighter $\delta^{30}$Si of bulk EC (Kadlag et al., 2019, this study).

In addition, the $\delta^{56}$Fe of five bulk EC analyzed in this study ($0.03 \pm 0.04$‰, $n = 5$) was found to be indistinguishable from that of OC and CC (Craddock & Dauphas, 2011; Poitrasson et al., 2004; Wang et al., 2014). The uniform $\delta^{56}$Fe among bulk chondrites further reflects that the light $\delta^{30}$Si of EC cannot be a sole

consequence of arbitrary addition of metal with extremely low $\delta^{30}Si$. This is because random accretion of isotopically variable metals is expected to generate scattered, non-chondritic $\delta^{56}Fe$ values in bulk EC, which is not observed. Given this rather tight constraint, it is clear that processes that led to the light Si isotope composition of bulk EC did not disturb their bulk Fe isotope compositions, which implies that Si isotopes were mostly fractionated before the accretion of EC parent body, probably in their reservoir stage. Previous studies have shown that the loss of isotopically heavier forsterite silicates from the EC-forming region could have contributed to the characteristically low Mg/Si and lighter $\delta^{30}Si$ of bulk EC compared to OC and CC (Dauphas et al., 2015; Kadlag et al., 2019). Since EH chondrites are depleted in refractory elements and Mg relative to Fe, Ni, and Si (as indicated by their low Al/Si of 0.60 and Mg/Si ratio of 0.73 (Wasson et al., 1988)), it is likely that the isotopically heavy forsterite-rich silicates were lost simultaneously with the refractory elements from the nebular region where EC parent bodies were formed (Dauphas et al., 2015; Kadlag et al., 2019).

### *Influence of Redox Conditions on Si and Fe Isotope Fractionation*

To access the significance of metal–silicate–sulfide partitioning in generating isotope fractionation in reduced versus oxidized planetary environments, we have carried out Si and Fe isotope analyses in the bulk and magnetic phase separates of Northwest Africa (NWA) 5492, which is a metal-enriched (>20 vol% metal) ungrouped chondrite, presumably from the inner solar system (Weisberg et al., 2012, 2015). The silicates of NWA 5492 are composed primarily of nearly pure enstatite and are more reduced than the silicates of OC and CC (Weisberg et al., 2012, 2015). The average $\delta^{30}Si$ of bulk NWA 5492 was found to be $-0.42 \pm 0.07‰$, which is indistinguishable from the Si isotope composition of CC and OC (average $\delta^{30}Si_{CC\text{-}OC} = -0.46 \pm 0.02‰$ (Zambardi et al., 2013)). In addition, no significant $\delta^{30}Si$ differences were observed between bulk NWA 5492 (i.e., $\delta^{30}Si_{BM} = -0.42 \pm 0.07‰$) and its NM fraction ($\delta^{30}Si_{NM} = -0.46 \pm 0.06‰$), which is in contrast to the Si isotope differences observed between bulk EC and its NM fraction (Table 1). This result can be explained by the fact that despite FeO-poor silicate minerals, the metals of NWA 5492 are not reduced enough to incorporate significant amounts of Si. Thus, due to negligible metal–silicate Si isotope fractionation in the formation region of NWA 5492, its bulk and NM fractions have preserved $\delta^{30}Si$ similar to that of OC and CC.

On the other hand, significant $\delta^{56}Fe$ variations exist between magnetic and NM fractions of NWA 5492. Iron in NWA 5492 is distributed among its silicate (composed dominantly of pyroxene with modal abundances of 44.7 vol%), sulfide (2.5 vol%), and Fe-Ni metal (modal abundances of 22.6 vol%) phases (Weisberg et al., 2012). The average Fe isotope composition was found to vary systematically from M to NM fractions in the following order: $\delta^{56}Fe_M$ ($0.206 \pm 0.065‰$) > $\delta^{56}Fe_{BM}$ ($0.042 \pm 0.046‰$) > $\delta^{56}Fe_{NM}$ ($-0.131 \pm 0.008‰$). The direction and magnitude of Fe isotope fractionation between magnetic and NM phases of NWA 5492, that is, $\Delta^{56}Fe_{M\text{-}NM} = 0.34 \pm 0.065‰$, overlap with the reported $\Delta^{56}Fe_{Metal\text{-}Troilite}$ of OC ($0.24 \pm 0.39‰$), EC ($0.26 \pm 0.04‰$, Qingzhen), pallasites (~0.28‰), and iron-meteorites ($0.32 \pm 0.23‰$, Odessa) (Needham et al., 2009; Wang et al., 2014; Weyer et al., 2005; Williams et al., 2006). Given this, our Fe isotope data of NWA 5492 suggest that stable Fe isotopes have undergone significant fractionation among its magnetic and NM phases in diverse meteorite groups irrespective of the physicochemical conditions and oxygen fugacity under which their last thermal processing and isotopic fractionation have occurred, which is not the case for Si isotopes.

A key feature observed upon comparing the Fe isotope composition of the matrix-derived magnetic fractions (i.e., matrix metals, MM) of the studied EC with that of two unequilibrated OCs and an ungrouped chondrite was the distinct Fe isotope composition of the two groups. The average $\delta^{56}Fe$ of the matrix metals of NWA 5492, WSG 95300, and QUE 97008 were $0.206 \pm 0.065‰$, $0.198 \pm 0.095‰$, and $0.286 \pm 0.062‰$, respectively. The average $\delta^{56}Fe$ values of the matrix metals of EC were $0.129 \pm 0.018‰$ (Kota-Kota), $0.130 \pm 0.032‰$ (Sahara 97072), $-0.023 \pm 0.053‰$ (MAC 88184), $0.032 \pm 0.026‰$ (Abee), and $0.140 \pm 0.046‰$ (Indarch). Although based on a small data set ($n = 8$), Student's $t$-tests indicate that the $\delta^{56}Fe$ values of the matrix metals of the studied OC and NWA 5492 (average $\delta^{56}Fe_{OC/UNG\_MM} = 0.230 \pm 0.097‰$) are significantly heavier compared to that of EC (average $\delta^{56}Fe_{EC\_MM} = 0.082 \pm 0.146‰$) at 95% confidence level. This observation can be explained by the fact that the matrix metals of EC often contain a significantly higher abundance of intergrown sulfides, which is reflected in their Ni/S ratio (ranges from 0.59 to 1.01) compared to that of OC and NWA 5492 (Ni/S >4, Table 2). Since sulfides are enriched in light Fe isotopes, its minor contribution can dramatically change the measured $\delta^{56}Fe$ of the studied phases. Given this, we suggest that the heavier $\delta^{56}Fe$ of the magnetic fractions of NWA 5492 and OC is probably because of the lesser abundance of intergrown sulfides in their metallic fractions compared to that in EC. To conclude, the significant Si isotope fractionation between metal and silicates in only restricted to highly reduced EC whereas stable Fe isotopes have

undergone fractionation between metal, troilite, and/or silicates in almost all undifferentiated meteorites.

### *Diffusion during Parent Body Metamorphism*

The chondrites analyzed in this study have a metamorphic grade of 3 (Sahara 97072, Kota-Kota, MAC 88184) and 4 (Abee, Indarch). Analyses of noble gases in presolar diamonds suggest that the maximum equilibration temperatures of EH3 and EH4 chondrites are ~800 and ~900 K, respectively (Huss & Lewis, 1994). At 900 K, the diffusion length of Si in enstatite is calculated to be $\sim 10^{-6}$ to $10^{-2}$ μm in case of internal heating for a time period of 100 Ma (Dohmen et al., 2002). At similar time-scale, the diffusion length of Si in Fe-Si metals is $\sim 10^{3}$ μm (Riihimäki et al., 2008), which implies that the rate of self-diffusion of Si in silicates is at least five times slower compared to that in metals. Thus, although the metallic fractions of EC are likely to have undergone Si diffusion during thermal metamorphism, diffusion of Si isotopes among the silicate minerals of unequilibrated ECs should not be highly effective. Diffusion slows down further at temperature of 800 K or below, and therefore, Si isotope equilibration during thermal metamorphism in chondrite parent body is not expected to alter the $\delta^{30}$Si values of the silicate phases of EH3 chondrites. Since silicates act as a major reservoir of Si in EC and it is difficult to diffuse Si in silicate minerals during planetary heating processes, the Si isotope variations observed among the silicate fractions of EH3 chondrites most likely preserve the Si isotope signatures of the gas and solid (silicate or metal) interaction processes in the reduced nebula.

Owing to the higher diffusivity of Fe relative to Si, the Fe isotopic composition of the metal and sulfide fractions of EC may have been affected by impact melting or radioactive heating of parent body if such late heating events had lasted for a longer period. At 900 K, the average Fe-Mg interdiffusion coefficient in orthopyroxenes is $10^{-26}$ m$^2$ s$^{-1}$ (Dohmen et al., 2016), which indicates that Fe diffusion in enstatite is extremely slow at 900 K. However, at similar temperature, the self-diffusion coefficients of Fe are larger in metals and sulfides, which vary from approximately $10^{-20}$ m$^2$ s$^{-1}$ in solid Fe-alloys (Zhang, 2014) to $10^{-9}$ m$^2$ s$^{-1}$ in ferrous sulfide (Condit et al., 1974). Therefore, isotope homogenization of a 50 μm solid iron alloy at 900 K requires a time-scale of approximately 1000 years, and it takes only few seconds for ferrous sulfides to re-equilibrate. Given this, if we consider diffusion distances to be on the order of 50–80 μm, diffusion is expected to re-equilibrate the Fe isotope distribution between metals and sulfides in planetary bodies during the time-scale of parent body metamorphism, that is, millions of years (Huss et al., 2006). Hence, we can state that the $\delta^{56}$Fe of metal and sulfide grains of the EC matrix might have re-equilibrated, partially or completely, as a result of heating processes on the parent body.

Summarizing this section, here we have shown that the EC components are characterized by significant metal–silicate Si isotope fractionation, and the overall lighter $\delta^{30}$Si of bulk EC compared to CC and OC can be attributed to the presence of light Si isotopes in its metallic phases and loss of heavier forsterite-rich silicates from the EC formation region. The slow self-diffusion of Si in enstatite reflects that the Si isotope composition of the silicate fractions of EH3 chondrite preserves information of nebular processing of the reduced EC–forming reservoir. On the other hand, the Fe isotopes in EC were mostly fractionated because of metal–sulfide Fe isotope partitioning. The higher diffusivity of Fe in sulfides suggest that the $\delta^{56}$Fe variations among EC components were most likely affected by parent body heating processes such as impact melting and metamorphism. We have also demonstrated that measurable Fe isotope fractionation always occurs between metal and sulfides during typical nebular and/or planetary processes irrespective of the oxygen fugacity of the region where parent body processes took place, whereas Si isotope fractionation between metal and silicates is strongly affected by the $fO_2$ of nebular region.

## Gas–Solid Interaction Processes in Reduced Nebular Environment

During the early stages of nebular evolution, processes such as evaporation, condensation, and gas–solid or gas–melt reactions generated important chemical fractionations, leading to chemical diversity among planetary bodies. In this section, we discuss how interaction of condensing solids with the surrounding reduced gas might have led to strong Si and Fe isotopic fractionation in the EC-forming region.

### *Silicon Isotope Evolution*

EH chondrites are rich in Si-bearing Fe-Ni metal and it is believed that Fe-Ni metals of the most primitive EC represent direct condensation products of the solar nebula (Campbell et al., 2005). Therefore, condensation of Fe-Ni metal is expected to have played a key role in the generation of the observed Si and Fe isotope fractionation in EH3 components. In both equilibrium and non-equilibrium situations, ab initio calculations have shown that Fe-Ni metals condensing from reduced SiO and SiS nebula should be significantly enriched in lighter Si isotopes whereas the silicate phases become isotopically heavier (Javoy et al., 2012), which is supported by the present and previous studies (Kadlag et al., 2019; Sikdar & Rai, 2020). Because parent-body processes cannot explain the Si isotope variations in EC

(see "Origin of Si and Fe Isotope Heterogeneity in EC" Section), the positive correlation between $\delta^{30}Si$ and Mg# (or Mg/Fe) (Figure 5) likely reflects metal–silicate Si isotope fractionation during nebular processes. Here, we investigate the formation conditions of EC components by utilizing the temperature dependency of stable isotope fractionation and the magnitude of Si isotope fractionation predicted between $SiO_{gas}$ and solid species (Javoy et al., 2012).

We assume that the condensed solids were in equilibrium with the surrounding gas and the $\delta^{30}Si$ values of the silicate phases of unequilibrated EH3 chondrites preserve pristine signatures of gas–solid interaction processes of the nebula (discussed in previous section). Considering the average $\delta^{30}Si$ of the silicate phases of EH3 chondrites to be $-0.43 \pm 0.25‰$ (calculated based on data obtained in this study; Fitoussi & Bourdon, 2012; Kadlag et al., 2019; Savage & Moynier, 2013; Sikdar & Rai, 2020) and the average mineral equilibration temperature of EH chondrites of $980 \pm 150$ K (Javoy et al., 2012), the $\delta^{30}Si$ of $SiO_{(gas)}$ of the EC-forming region can be estimated to be $-4.8 \pm 0.6‰$ (Appendix A). This $\delta^{30}Si$ value of $SiO_{(gas)}$ is expected to be already fractionated due to forsterite condensation because when forsterite fully condenses, approximately half of Si remains in the gaseous phase and the rest is in forsterite with $\delta^{30}Si_{Forsterite}$ of $+0.71‰$, suggesting an important role of the removal of heavy Si isotope-rich forsterite precursors in the generation of lighter Si isotope composition of bulk EC (Dauphas et al., 2015). As enstatites are mostly formed from the residual gas left after forsterite condensation, the episode of forsterite removal must have occurred before EC formation.

Now we consider the EC components that display the most extreme $\delta^{30}Si$ values, that is, the Fe-Ni metals and the WMP silicates. In case of metals, we have not restricted our calculations to MSNs because their $\delta^{30}Si$ could be associated with magmatic processes on differentiated bodies (Horstmann et al., 2014), and thus, MSNs might not record condensation processes. Rather, we have considered the mean Si isotope composition of bulk Fe-Ni metals of EH3 chondrites (i.e., $-6 \pm 0.3‰$), which has been estimated by averaging the $\delta^{30}Si$ values of EC metals (ranging from $-8.24 \pm 0.12‰$ to $-4.11 \pm 0.13‰$) acquired in this study and literature data (Kadlag et al., 2019; Sikdar & Rai, 2020). For $\delta^{30}Si_{EH3\ Metal}$ of $-6 \pm 0.3‰$, the magnitude of $\Delta^{30}Si_{Metals\text{-}SiO(gas)}$ requires that the metals of EH3 chondrites were condensed at a higher temperature of $1200 \pm 200$ K (Appendix B). Next, we consider the WMPs from Sahara 97072 ($\delta^{30}Si_{WMPs} = +0.23 \pm 0.10‰$) that display the heaviest $\delta^{30}Si$ values (Table 1). As discussed earlier, cristobalite or amorphous $SiO_2$ should represent the main constituent mineral of the WMPs. In a gas of solar composition, silicon monoxide (SiO) is the dominant silicon-bearing molecule (Chaussidon et al., 2008; Javoy et al., 2010, 2012), and $SiO_2$ can condense in the EC-forming region through disproportionation of SiO (Javoy et al., 2012):

$$2SiO \rightarrow SiO_2 + Si_{Fe-metal} \quad (2)$$

Considering $\delta^{30}Si_{SiO(gas)}$ to be $-4.8 \pm 0.6‰$, the $\delta^{30}Si$ of WMPs of Sahara 97072 ($+0.23 \pm 0.10‰$) requires that these phases were formed by equilibrium condensation from the solar nebula at a lower temperature of $960 \pm 50$ K (Appendix C). At this temperature, $SiO_2$ was probably condensed from the reduced, supersaturated gas left after the condensation of metals at higher temperatures. Given this, our Si isotope data suggests that the Fe-Ni metals of EC-forming region were condensed earlier than the isotopically heavier silicates, lending support to the EC formation models that have argued for substantial differences in condensation temperature of metals and silicates/oxides at high-C/O nebular environments (Larimer & Bartholomay, 1979). We emphasize that this conclusion assumes that the EC components underwent equilibrium Si isotope fractionation between gas and condensed solids in the nebula. However, the decoupling between $\delta^{30}Si$ and Mg/Fe ratio among EC silicates requires that kinetic effects, probably during cooling of chondrules and dust particles, might have played a role as well in the generation of the observed Si isotope fractionation in EC (Kadlag et al., 2019). To add, the light Si isotope enrichments ($\delta^{30}Si$ ranging from $-9‰$ to $-1‰$) of Mg-rich olivine grains in amoeboid olivine aggregates (AOAs) of CC (Marrocchi et al., 2019) are at odds with the positive 2‰/amu fractionation expected from olivine-gas equilibrium scenario (Dauphas et al., 2015; Javoy et al., 2012), thereby hinting towards kinetic fractionations during condensation and gas–melt interactions in the formation region of CC. However, the magnitude to which kinetically controlled Si isotope fractionation has affected the EC components is not yet known and can be evaluated by Si isotope analyses in olivine separates of EH3 chondrites.

### *Iron Isotope Evolution*

Although the Fe isotope fractionation observed in EC components was influenced by parent body heating processes (discussed in "Diffusion During Parent Body Metamorphism" Section), nebular Fe isotope fractionation should be also measurable. At the maximum metamorphic temperatures estimated for EH3 and EH4 chondrites of 800–900 K (Huss & Lewis, 1994), the expected values of $\Delta^{56}Fe_{metal-sulfide}$ ($=\delta^{56}Fe_{magnetic} - \delta^{56}Fe_{non\text{-}magnetic}$) range from $0.28 \pm 0.02‰$ to $0.22 \pm$

0.03‰, respectively (calculated based on fractionation factors predicted by theoretical calculations (Polyakov et al., 2007, Equation 3)).

$$\Delta^{56}Fe_{metal-sulfide} = \frac{0.1774 \times 10^6}{T^2} + \frac{5.6912 \times 10^9}{T^4} + \frac{0.2605 \times 10^{12}}{T^6} \quad (3)$$

The metal–sulfide Fe isotope fractionation ($\Delta^{56}Fe_{metal-sulfide}$) of EC determined in this study ranges from 0.25‰ to 0.39‰. If we consider $\Delta^{56}Fe_{metal-sulfide}$ of $0.25 \pm 0.04$‰, the Fe isotope difference suggests that the metals and sulfides were equilibrated at a temperature of ~$850 \pm 100$ K. The $\Delta^{56}Fe_{metal-sulfide}$ of $0.39 \pm 0.05$‰, however, requires that metal–sulfide equilibration occurred at lower temperature of $700 \pm 50$ K. Although the lower limit of $\Delta^{56}Fe_{metal-sulfide}$ in EC (0.25‰) overlaps with the equilibrium metal–sulfide Fe isotope fractionation factors predicted by theoretical calculations at 800–900 K (Polyakov et al., 2007; Polyakov & Soultanov, 2011), its upper limit (i.e., 0.39‰) is larger than the theoretical predictions. These results illustrate that kinetic processes during planetary metamorphism or during repeated heating and cooling episodes of chondrule formation have modified any possible equilibrium Fe isotope fractionation inherited from the nebula. Overall, we suggest that the Si and Fe isotopic composition of ECs was affected by a range of physicochemical conditions that prevailed during early nebular evolution.

## Homogeneous $\delta^{56}$Fe of the Solar System

Despite the relatively strong Fe isotope heterogeneity among different EC components (ranging from $-0.305 \pm 0.077$‰ to $0.196 \pm 0.038$‰), the Fe isotope composition of the five bulk EC ($0.03 \pm 0.04$‰, $n = 5$) analyzed in this study overlaps with the $\delta^{56}$Fe of diverse types of bulk chondrites (EH, EL, Ungr, H, L, LL, CV, CM, and CI) and most achondrites (HEDs, SNCs, Ureilites, Brachinites), Figure 9 (Needham et al., 2009; Poitrasson et al., 2004; Wang et al., 2013, 2014; Weyer et al., 2005). In the Fe–Si isotope space (Figure 9), most planetary materials cluster at $\delta^{56}$Fe of ~0.0‰ (Craddock & Dauphas, 2011; Poitrasson et al., 2004; Weyer et al., 2005), with the exception of aubrites, volatile-depleted angrites, and lunar igneous rocks (Pringle et al., 2014; Wang et al., 2012). The Fe isotope composition of the later may have been affected by igneous differentiation processes or evaporative loss of light Fe isotopes during the magma ocean stage (Pringle et al., 2014). We found that the $\delta^{56}$Fe of ungrouped NWA 5492 is also indistinguishable from bulk planetary materials, which support previous conclusions that Fe isotopes were already well homogenized in the early nebula before the onset of planetesimal accretion (Zhu et al., 2001). Such homogeneity in $\delta^{56}$Fe rules out any significant redistribution and mixing of isotopically fractionated Fe phases such as metals, sulfides, or chondrules across the proto-planetary disk prior to the formation of their parent bodies (Johansen et al., 2021). This is because to maintain chondritic $\delta^{56}$Fe in diverse types of bulk planetary materials from variable heliocentric distances, the isotopically distinct Fe phases need to be redistributed in a very specific proportion, for which no evidence exists. Instead, the homogeneous $\delta^{56}$Fe suggest that during local heating and cooling cycles, the metals, silicates, and sulfides were retained in their local nebular domains. Thus, we can suggest that the solar system bodies that display homogeneous and chondritic $\delta^{56}$Fe, yet variable compositional characteristics (e.g., variations in the abundance of refractory elements, volatile depletion pattern, or specific mass-independent isotope composition) likely represent planetesimals that were accreted from local feeding zones in the disk. Assuming rapid initial growth of planetesimals in these feeding zones, the proposed narrow gaps and fine-scale ring structures in the disk (Izidoro et al., 2021) must have existed after the partial or entire condensation of Fe in the inner solar system and before the episodes of gas dissipation. During this time, the lateral mixing between inner and outer solar system dust remained limited, either because of the growth of Jupiter (Batygin & Laughlin, 2015; Kruijer et al., 2017) or because of the changing dynamics of the proto-planetary disk (Lichtenberg et al., 2021). Due to such restricted movements, the chondritic components were probably retained in spatially restricted feeding zones. Overall, we suggest that the significant Fe isotope fractionation observed among EC components must be an outcome of local thermal processing at a range of physicochemical conditions in the nebula and/or in the parent body.

## Implications for Silicon and Iron Isotope Composition of the Earth

The Si isotope composition of the BSE is heavier than chondrites by at least ~0.1‰ (Armytage et al., 2011; Fitoussi & Bourdon, 2012; Georg et al., 2007; Zambardi et al., 2013). Three major processes are considered as possible explanation: (i) Equilibrium Si isotope fractionation between metal and silicate during core–mantle segregation (Armytage et al., 2011; Georg et al., 2007; Zambardi et al., 2013), (ii) preferential evaporation of light Si isotopes into space during vapor loss from molten planetesimal precursors (Hin et al., 2017; Pringle et al., 2014), and (iii) Si isotope fractionation associated with interaction between gaseous SiO and solid forsterite

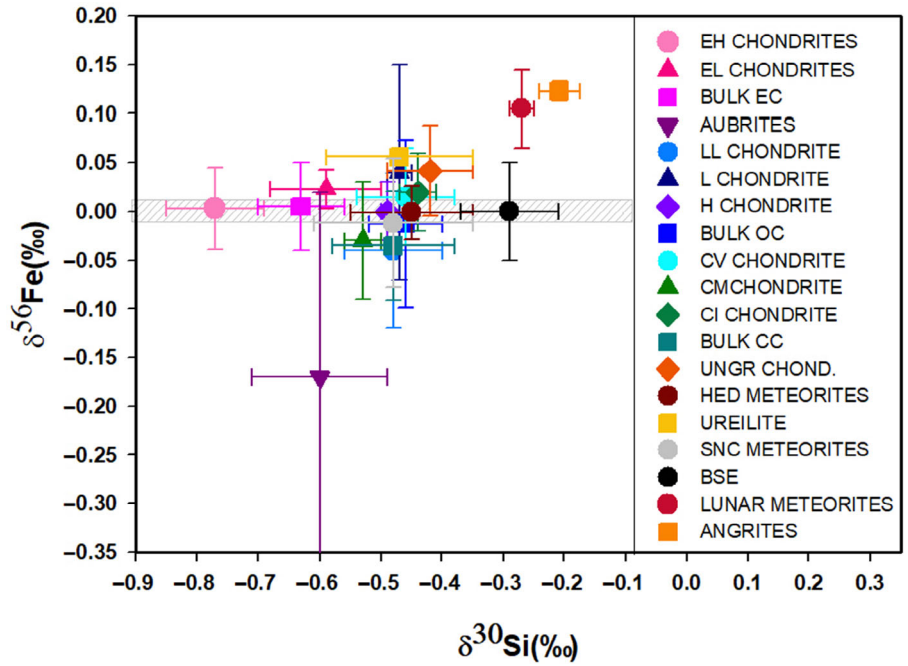


FIGURE 9. Si and Fe isotope composition of diverse planetary materials compiled from published data (Armytage et al., 2011; Barrat et al., 2015; Dauphas et al., 2015; Fitoussi & Bourdon, 2012; Needham et al., 2009; Savage et al., 2010; Savage & Moynier, 2013; Wang et al., 2012, 2013, 2014; Weyer et al., 2005; Zambardi et al., 2013) and results of EC from this study. In Si-Fe isotope space of bulk planetary materials, most Fe isotope data cluster at around ±0.00‰ whereas Si isotope values display heterogeneous distribution. The larger uncertainty in the $\delta^{56}$Fe value of Aubrites is due to significant Fe isotope difference between main group aubrite and Shallowater meteorite. (Color figure can be viewed at wileyonlinelibrary.com)

in the nebula (Dauphas et al., 2015; Kadlag et al., 2019). The second and the third processes may involve a combination of metal–silicate Si isotope fractionation at nebular conditions and evaporative loss of light Si isotopes into space during high-energy collisions among growing planetesimals (Sikdar & Rai, 2020).

Chemical accretion and core formation models of terrestrial planets hypothesize that the Earth underwent heterogeneous accretion, with the initially accreting materials being similar to highly reduced EC (Rubie et al., 2015; Wood et al., 2006). Given the chondritic to superchondritic $\delta^{30}$Si of EC silicates, it is likely that heterogeneous accretion of EC silicates after the aggregation of a light Si-enriched metallic proto-core can explain the heavier $\delta^{30}$Si of BSE without requiring any significant Si isotope fractionation at high-temperature core-forming conditions. However, the formation of the mantle of a large terrestrial planet like the Earth without equilibration with its core is not a feasible scenario. In addition, BSE has a considerably larger abundance of forsterite and a higher Mg/Si ratio of 1.25 (McDonough & Sun, 1995) compared to that of EC silicates, which makes it unlikely that materials similar to EC silicates were solely responsible for the current Si isotope and chemical composition of the BSE. Since the similar nucleosynthetic isotope composition between BSE and EC for several elements indicates accretion of EC parent bodies and the Earth from the same isotopic reservoir of the solar system (Dauphas, 2017), a viable explanation for the characteristic Si isotope and elemental composition of the BSE can be provided by the formation of the silicate reservoir of the Earth via accretion of (i) silicates similar to that of EC and (ii) unsampled inner solar system materials lost from the EC-forming or nearby regions that were enriched in heavy Si isotopes and refractory lithophile elements (see "Nebular Origin of the Lighter $\delta^{30}$Si of Bulk EC" Section of this study).

Similar to Si isotopes, the heavier Fe isotope composition of terrestrial basalts relative to chondrites by ~0.1‰ has been interpreted to reflect either metal–silicate equilibrium Fe isotope fractionation during core–mantle segregation, or evaporative loss of light Fe isotopes during impact erosion, or isotope fractionation during partial mantle melting and fractional crystallization (Poitrasson et al., 2004; Polyakov, 2009; Schoenberg & Blanckenburg, 2006; Sossi & Moynier, 2017). Although terrestrial basalts have a non-chondritic $\delta^{56}$Fe, the stable Fe isotope composition of fertile mantle peridotites is indistinguishable from bulk chondrites (Craddock et al., 2013; Wang et al., 2013; Weyer & Ionov, 2007). Since

the heavier $\delta^{56}$Fe of terrestrial basalts relative to peridotites could be generated during partial melting and fractional crystallization (Weyer et al., 2005; Weyer & Ionov, 2007), it is likely that the chondritic Fe isotope composition of mantle peridotites was not significantly affected by post-nebular processes. Given this, we conclude that the governing reactions that fractionated Earth's Si and Fe isotope composition was mostly set at nebular temperature–pressure conditions, possibly through metal–silicate–sulfide–gas phase fractionation and removal of refractory components, and the Earth has mostly inherited its Si and Fe isotopic signature predominantly from the mixture of its precursor materials. This would in turn imply that the Si and Fe isotope composition of the BSE has not been significantly modified by high temperature–pressure core–mantle equilibration of the Earth.

## CONCLUSIONS

The physically separated components of EH3 and EH4 enstatite chondrites display considerable mass-dependent Si and Fe isotope fractionation, which is partly affected by incomplete separation of different chondrite phases and predominantly reflects nebular/parent body processes. The correlated variation between (i) $\delta^{30}$Si and Mg# and (ii) $\delta^{56}$Fe and Ni/S among EC components coupled with the (iii) inverse correlation between $\delta^{30}$Si and $\delta^{56}$Fe suggest that metal–silicate Si isotope partitioning and metal–sulfide Fe isotope partitioning at low oxygen fugacity provides a first-order explanation of the observed isotope variations in EC components. The Fe isotope distribution in EH3 and EH4 chondrites was affected by late diffusive exchange of Fe isotopes during parent body heating processes whereas the $\delta^{30}$Si values of their silicate phases mostly preserves nebular signature. Fe isotope analyses in magnetic phase separates of two OC, an ungrouped chondrite, and published data on chondrites show that Fe isotopes have undergone considerable metal–sulfide fractionation in most planetary bodies irrespective of the oxygen fugacity under which their parent planets were accreted, which is not the case for Si isotopes. The relatively strong Fe isotope fractionation between metals and sulfides during nebular and parent body processes is in contrast with the homogeneous $\delta^{56}$Fe of bulk planetary materials from different domains of the proto-planetary disk, indicating that arbitrary mixing of chondrules with troilite and metals from various heliocentric distances is not a feasible accretion scenario. The observation further illustrates that the components of a particular planetesimal were formed and retained in spatially restricted feeding zones, and the Fe isotope fractionation observed between metals and sulfides mostly reflect local changes in the physicochemical conditions of their evolutionary environments. Another corollary of the uniform $\delta^{56}$Fe among bulk chondrites is that the light $\delta^{30}$Si of EH3 chondrites cannot be a sole consequence of arbitrary addition of metal with extremely low $\delta^{30}$Si because this would have led to scattered, non-chondritic $\delta^{56}$Fe in bulk EC, which is not observed. Rather, the lighter $\delta^{30}$Si of EH chondrites must be a property of the protoplanetary disk where EC parent bodies were formed. It is likely that early loss of isotopically heavier refractory silicates has influenced the end-member Si isotope compositions of EH3 and EH4 chondrites. Our Si and Fe isotope data in EC components suggest that the characteristic isotope signature of the Bulk Silicate Earth was carried over from its precursor materials, whereby the isotopically heavier EC silicates and forsterite-rich refractory silicates lost from the EC-forming regions could have contributed to the growing silicate Earth. The accretion of such refractory components can explain not only the heavier $\delta^{30}$Si of BSE but also its higher Mg/Si ratio and enriched refractory element abundances.

*Acknowledgments*—J. Sikdar was funded by a fellowship of TRR 170 (DFG, German Research Foundation–#263649064–TRR 170). The US Museum of Natural History Washington D.C., the Field Museum Chicago, ANSMET, Senckenberg Museum Frankfurt, and the Natural History Museum London are acknowledged for providing samples. We thank F. von Blanckenburg and GFZ for laboratory infrastructure support; J. Buhk, P. Gleißner, E. Hoffmann, Y. Kadlag, and J. Schlegel for technical help; and Y. Kadlag and N. Dauphas for discussions. This is TRR 170 publication no. 189. Open Access funding enabled and organized by Projekt DEAL.

*Data Availability Statement*—Most of the important data obtained in this study have been provided in the data tables. Other data can be obtained upon request from the corresponding author.

*Editorial Handling*—Dr. Gopalan Srinivasan

## REFERENCES

Allègre, C. J., Poirier, J.-P., Humler, E., and Hofmann, A. W. 1995. The Chemical Composition of the Earth. *Earth and Planetary Science Letters* 134: 515–26.

Armytage, R. M. G., Georg, R. B., Savage, P. S., Williams, H. M., and Halliday, A. N. 2011. Silicon Isotopes in Meteorites and Planetary Core Formation. *Geochimica et Cosmochimica Acta* 75: 3662–76.

Barrat, J. A., Rouxel, O., Wang, K., Moynier, F., Yamaguchi, A., Bischoff, A., and Langlade, J. 2015. Early Stages of Core Segregation Recorded by Fe Isotopes in an Asteroidal Mantle. *Earth and Planetary Science Letters* 419: 93–100.

Batygin, K., and Laughlin, G. 2015. Jupiter's Decisive Role in the Inner Solar System's Early Evolution. *Proceedings of the National Academy of Sciences of the United States of America* 112: 4214–7.

Birch, F. 1964. Density and Composition of Mantle and Core. *Journal of Geophysical Research (1896–1977)* 69: 4377–88.

Campbell, A. J., Petaev, M. I., Meibom, A., Perron, C., and Zanda, B. 2005. Origin and Thermal History of FeNi-Metal in Primitive Chondrites. *Chondrites and Protoplanetary Disk ASP Conference Series* 341: 407–31.

Cartier, C., Hammouda, T., Doucelance, R., Boyet, M., Devidal, J.-L., and Moine, B. 2014. Experimental Study of Trace Element Partitioning Between Enstatite and Melt in Enstatite Chondrites at Low Oxygen Fugacities and 5GPa. *Geochimica et Cosmochimica Acta* 130: 167–87.

Chabot, N. L., Wollack, E. A., McDonough, W. F., Ash, R. D., and Saslow, S. A. 2017. Experimental Determination of Partitioning in the Fe-Ni System for Applications to Modeling Meteoritic Metals. *Meteoritics & Planetary Science* 52: 1133–45.

Chaussidon, M., Libourel, G., and Krot, A. N. 2008. Oxygen Isotopic Constraints on the Origin of Magnesian Chondrules and on the Gaseous Reservoirs in the Early Solar System. *Geochimica et Cosmochimica Acta* 72: 1924–38.

Chen, X., Lapen, T. J., and Chafetz, H. S. 2017. Accurate and Precise Silicon Isotope Analysis of Sulfur- and Iron-Rich Samples by MC-ICP-MS. *Geostandards and Geoanalytical Research* 41: 427–35.

Condit, R. H., Hobbins, R. R., and Birchenall, C. E. 1974. Self-Diffusion of Iron and Sulfur in Ferrous Sulfide. *Oxidation of Metals* 8: 409–55.

Craddock, P. R., and Dauphas, N. 2011. Iron Isotopic Compositions of Geological Reference Materials and Chondrites. *Geostandards and Geoanalytical Research* 35: 101–23.

Craddock, P. R., Warren, J. M., and Dauphas, N. 2013. Abyssal Peridotites Reveal the Near-Chondritic Fe Isotopic Composition of the Earth. *Earth and Planetary Science Letters* 365: 63–76.

Dauphas, N. 2017. The Isotopic Nature of the Earth's Accreting Material through Time. *Nature* 541: 521–4.

Dauphas, N., Poitrasson, F., Burkhardt, C., Kobayashi, H., and Kurosawa, K. 2015. Planetary and Meteoritic Mg/Si and δ30Si Variations Inherited from Solar Nebula Chemistry. *Earth and Planetary Science Letters* 427: 236–48.

Dohmen, R., Chakraborty, S., and Becker, H.-W. 2002. Si and O Diffusion in Olivine and Implications for Characterizing Plastic Flow in the Mantle. *Geophysical Research Letters* 29: 26-21–4.

Dohmen, R., Ter Heege, J. H., Becker, H.-W., and Chakrabortrty, S. 2016. Fe-Mg Interdiffusion in Orthopyroxene. *American Mineralogist* 101: 2210–21.

Drake, M. J., and Righter, K. 2002. Determining the Composition of the Earth. *Nature* 416: 39–44.

El Goresy, A., Lin, Y., Miyahara, M., Gannoun, A., Boyet, M., Ohtani, E., Gillet, P., et al. 2017. Origin of EL3 Chondrites: Evidence for Variable C/O Ratios during their Course of Formation—A State of the Art Scrutiny. *Meteoritics & Planetary Science* 52: 781–806.

Fischer-Gödde, M., Elfers, B. M., Münker, C., Szilas, K., Maier, W. D., Messling, N., Morishita, T., Van Kranendonk, M., and Smithies, H. 2020. Ruthenium Isotope Vestige of Earth's Pre-Late-Veneer Mantle Preserved in Archaean Rocks. *Nature* 579: 240–4.

Fitoussi, C., and Bourdon, B. 2012. Silicon Isotope Evidence against an Enstatite Chondrite Earth. *Science* 335: 1477–80.

Georg, R. B., Halliday, A. N., Schauble, E. A., and Reynolds, B. C. 2007. Silicon in the Earth's Core. *Nature* 447: 1102–6.

Georg, R. B., Reynolds, B. C., Frank, M., and Halliday, A. N. 2006. New Sample Preparation Techniques for the Determination of Si Isotopic Compositions Using MC-ICPMS. *Chemical Geology* 235: 95–104.

Gessmann, C. K., Wood, B. J., Rubie, D. C., and Kilburn, M. R. 2001. Solubility of Silicon in Liquid Metal at High Pressure: Implications for the Composition of the Earth's Core. *Earth and Planetary Science Letters* 184: 367–76.

Grossman, L., Simon, S. B., Rai, V. K., Thiemens, M. H., Hutcheon, I. D., Williams, R. W., Galy, A., et al. 2008. Primordial Compositions of Refractory Inclusions. *Geochimica et Cosmochimica Acta* 72: 3001–21.

Hezel, D. C., Poole, G. M., Hoyes, J., Coles, B. J., Unsworth, C., Albrecht, N., Smith, C., et al. 2015. Fe and O Isotope Composition of Meteorite Fusion Crusts: Possible Natural Analogues to Chondrule Formation? *Meteoritics & Planetary Science* 50: 229–42.

Hin, R. C., Coath, C. D., Carter, P. J., Nimmo, F., Lai, Y.-J., Pogge von Strandmann, P. A. E., Willbold, M., Leinhardt, Z. M., Walter, M. J., and Elliott, T. 2017. Magnesium Isotope Evidence that Accretional Vapour Loss Shapes Planetary Compositions. *Nature* 549: 511–5.

Hin, R. C., Fitoussi, C., Schmidt, M. W., and Bourdon, B. 2014. Experimental Determination of the Si Isotope Fractionation Factor between Liquid Metal and Liquid Silicate. *Earth and Planetary Science Letters* 387: 55–66.

Horstmann, M., Humayun, M., and Bischoff, A. 2014. Clues to the Origin of Metal in Almahata Sitta EL and EH Chondrites and Implications for Primitive E Chondrite Thermal Histories. *Geochimica et Cosmochimica Acta* 140: 720–44.

Huss, G., Rubin, A., and Grossman, J. 2006. Thermal Metamorphism in Chondrites. *Meteorites and the Early Solar System II* 943: 567–86.

Huss, G. R., and Lewis, R. S. 1994. Noble Gases in Presolar Diamonds II: Component Abundances Reflect Thermal Processing. *Meteoritics* 29: 811–29.

Izidoro, A., Dasgupta, R., Raymond, S. N., Deienno, R., Bitsch, B., and Isella, A. 2021. Planetesimal Rings as the Cause of the Solar System's Planetary Architecture. *Nature Astronomy* 6: 357–66. https://doi.org/10.1038/s41550-021-01557-z.

Javoy, M., Balan, E., Méheut, M., Blanchard, M., and Lazzeri, M. 2012. First-Principles Investigation of Equilibrium Isotopic Fractionation of O- and Si-Isotopes between Refractory Solids and Gases in the Solar Nebula. *Earth and Planetary Science Letters* 319–320: 118–27.

Javoy, M., Kaminski, E., Guyot, F., Andrault, D., Sanloup, C., Moreira, M., Labrosse, S., et al. 2010. The Chemical Composition of the Earth: Enstatite Chondrite Models. *Earth and Planetary Science Letters* 293: 259–68.

Johansen, A., Ronnet, T., Bizzarro, M., Schiller, M., Lambrechts, M., Nordlund, Å., and Lammer, H. 2021. A Pebble Accretion Model for the Formation of the Terrestrial Planets in the Solar System. *Science advances* 7: eabc0444.

Kadlag, Y., Tatzel, M., Frick, D. A., and Becker, H. 2019. The Origin of Unequilibrated EH Chondrites—Constraints

from in Situ Analysis of Si Isotopes, Major and Trace Elements in Silicates and Metal. *Geochimica et Cosmochimica Acta* 267: 300–21.

Kallemeyn, G. W., and Wasson, J. T. 1986. Compositions of Enstatite (EH3, EH4,5 and EL6) Chondrites: Implications Regarding their Formation. *Geochimica et Cosmochimica Acta* 50: 2153–64.

Kruijer, T. S., Burkhardt, C., Budde, G., and Kleine, T. 2017. Age of Jupiter Inferred from the Distinct Genetics and Formation Times of Meteorites. *Proceedings of the National Academy of Sciences of the United States of America* 114: 6712–6.

Larimer, J. W., and Bartholomay, M. 1979. The Role of Carbon and Oxygen in Cosmic Gases: Some Applications to the Chemistry and Mineralogy of Enstatite Chondrites. *Geochimica et Cosmochimica Acta* 43: 1455–66.

Lehner, S. W., McDonough, W. F., and Németh, P. 2014. EH3 Matrix Mineralogy with Major and Trace Element Composition Compared to Chondrules. *Meteoritics & Planetary Science* 49: 2219–40.

Lichtenberg, T., Drżkowska, J., Schönbächler, M., Golabek Gregor, J., and Hands Thomas, O. 2021. Bifurcation of Planetary Building Blocks during Solar System Formation. *Science* 371: 365–70.

Lin, Y., and Kimura, M. 1998. Petrographic and Mineralogical Study of New EH Melt Rocks and a New Enstatite Chondrite Grouplet. *Meteoritics & Planetary Science* 33: 501–11.

Marrocchi, Y., Villeneuve, J., Jacquet, E., Piralla, M., and Chaussidon, M. 2019. Rapid Condensation of the First Solar System Solids. *Proceedings of the National Academy of Sciences of the United States of America* 116: 23461–6.

McDonough, W. F., and Sun, S. 1995. The Composition of the Earth. *Chemical Geology* 120: 223–53.

Needham, A. W., Porcelli, D., and Russell, S. S. 2009. An Fe Isotope Study of Ordinary Chondrites. *Geochimica et Cosmochimica Acta* 73: 7399–413.

Oelze, M., Schuessler, J. A., and von Blanckenburg, F. 2016. Mass Bias Stabilization by Mg Doping for Si Stable Isotope Analysis by MC-ICP-MS. *Journal of Analytical Atomic Spectrometry* 31: 2094–100.

Palme, H., and O'Neill, H. S. C. 2014. 3.1—Cosmochemical Estimates of Mantle Composition. In *Treatise on Geochemistry*, edited by H. D. Holland, and K. K. Turekian, 2nd ed., 1–39. Oxford: Elsevier.

Patzer, A., SchlÜTer, J., Schultz, L., Tarkian, M., Hill, D. H., and Boynton, W. V. 2004. New Findings for the Equilibrated Enstatite Chondrite Grein 002. *Meteoritics & Planetary Science* 39: 1555–75.

Piani, L., Marrocchi, Y., Rigaudier, T., Vacher, L. G., Thomassin, D., and Marty, B. 2020. Earth's Water May Have Been Inherited from Material Similar to Enstatite Chondrite Meteorites. *Science* 369: 1110–3.

Poitrasson, F., Halliday, A. N., Lee, D.-C., Levasseur, S., and Teutsch, N. 2004. Iron Isotope Differences between Earth, Moon, Mars and Vesta as Possible Records of Contrasted Accretion Mechanisms. *Earth and Planetary Science Letters* 223: 253–66.

Polyakov, V. B. 2009. Equilibrium Iron Isotope Fractionation at Core-Mantle Boundary Conditions. *Science* 323: 912–4.

Polyakov, V. B., Clayton, R. N., Horita, J., and Mineev, S. D. 2007. Equilibrium Iron Isotope Fractionation Factors of Minerals: Reevaluation from the Data of Nuclear Inelastic Resonant X-Ray Scattering and Mössbauer Spectroscopy. *Geochimica et Cosmochimica Acta* 71: 3833–46.

Polyakov, V. B., and Soultanov, D. M. 2011. New Data on Equilibrium Iron Isotope Fractionation among Sulfides: Constraints on Mechanisms of Sulfide Formation in Hydrothermal and Igneous Systems. *Geochimica et Cosmochimica Acta* 75: 1957–74.

Pringle, E. A., Moynier, F., Savage, P. S., Badro, J., and Barrat, J.-A. 2014. Silicon Isotopes in Angrites and Volatile Loss in Planetesimals. *Proceedings of the National Academy of Sciences of the United States of America* 111: 17029–32.

Riihimäki, I., Virtanen, A., Pusa, P., Salamon, M., Mehrer, H., and Räisänen, J. 2008. Si Self-Diffusion in Cubic B20-Structured FeSi. *EPL (Europhysics Letters)* 82: 66005.

Ringwood, A. E. 1960. Silicon in the Metal Phase of Enstatite Chondrites. *Nature* 186: 465–6.

Rubie, D. C., Frost, D. J., Mann, U., Asahara, Y., Nimmo, F., Tsuno, K., Kegler, P., Holzheid, A., and Palme, H. 2011. Heterogeneous Accretion, Composition and Core–Mantle Differentiation of the Earth. *Earth and Planetary Science Letters* 301: 31–42.

Rubie, D. C., Jacobson, S. A., Morbidelli, A., O'Brien, D. P., Young, E. D., de Vries, J., Nimmo, F., Palme, H., and Frost, D. J. 2015. Accretion and Differentiation of the Terrestrial Planets with Implications for the Compositions of Early-Formed Solar System Bodies and Accretion of Water. *Icarus* 248: 89–108.

Saunier, G., Poitrasson, F., Moine, B., Gregoire, M., and Seddiki, A. 2010. Effect of Hot Desert Weathering on the Bulk-Rock Iron Isotope Composition of L6 and H5 Ordinary Chondrites. *Meteoritics & Planetary Science* 45: 195–209.

Savage, P. S., Georg, R. B., Armytage, R. M. G., Williams, H. M., and Halliday, A. N. 2010. Silicon Isotope Homogeneity in the Mantle. *Earth and Planetary Science Letters* 295: 139–46.

Savage, P. S., and Moynier, F. 2013. Silicon Isotopic Variation in Enstatite Meteorites: Clues to their Origin and Earth-Forming Material. *Earth and Planetary Science Letters* 361: 487–96.

Schauble, E. A. 2004. Applying Stable Isotope Fractionation Theory to New Systems. *Reviews in Mineralogy and Geochemistry* 55: 65–111.

Schauble, E. A., Rossman, G. R., and Taylor, H. P. 2001. Theoretical Estimates of Equilibrium Fe-Isotope Fractionations from Vibrational Spectroscopy. *Geochimica et Cosmochimica Acta* 65: 2487–97.

Schoenberg, R., and Blanckenburg, F. 2006. Modes of Planetary-Scale Fe Isotope Fractionation. *Earth and Planetary Science Letters* 252: 342–59.

Schoenberg, R., and von Blanckenburg, F. 2005. An Assessment of the Accuracy of Stable Fe Isotope Ratio Measurements on Samples with Organic and Inorganic Matrices by High-Resolution Multicollector ICP-MS. *International Journal of Mass Spectrometry* 242: 257–72.

Schuessler, J. A., Kämpf, H., Koch, U., and Alawi, M. 2016. Earthquake Impact on Iron Isotope Signatures Recorded in Mineral Spring Water. *Journal of Geophysical Research: Solid Earth* 121: 8548–68.

Schuessler, J. A., Schoenberg, R., Behrens, H., and von Blanckenburg, F. 2007. The Experimental Calibration of the Iron Isotope Fractionation Factor between Pyrrhotite and Peralkaline Rhyolitic Melt. *Geochimica et Cosmochimica Acta* 71: 417–33.

Scott, E. R. D., and Krot, A. N. 2007. 1.07—Chondrites and their Components. In *Treatise on Geochemistry*, edited by H. D. Holland, and K. K. Turekian, 1–72. Oxford: Pergamon.

Scott, E. R. D., and Krot, A. N. 2014. 1.2—Chondrites and their Components. In *Treatise on Geochemistry*, edited by H. D. Holland, and K. K. Turekian, 2nd ed., 65–137. Oxford: Elsevier.

Shahar, A., Hillgren, V. J., Horan, M. F., Mesa-Garcia, J., Kaufman, L. A., and Mock, T. D. 2015. Sulfur-Controlled Iron Isotope Fractionation Experiments of Core Formation in Planetary Bodies. *Geochimica et Cosmochimica Acta* 150: 253–64.

Shahar, A., Hillgren, V. J., Young, E. D., Fei, Y., Macris, C. A., and Deng, L. 2011. High-Temperature Si Isotope Fractionation between Iron Metal and Silicate. *Geochimica et Cosmochimica Acta* 75: 7688–97.

Sikdar, J., and Rai, V. K. 2017. Simultaneous Chromatographic Purification of Si and Mg for Isotopic Analyses Using MC-ICPMS. *Journal of Analytical Atomic Spectrometry* 32: 822–33.

Sikdar, J., and Rai, V. K. 2020. Si-Mg Isotopes in Enstatite Chondrites and Accretion of Reduced Planetary Bodies. *Scientific Reports* 10: 1273.

Sossi, P. A., and Moynier, F. 2017. Chemical and Isotopic Kinship of Iron in the Earth and Moon Deduced from the Lunar Mg-Suite. *Earth and Planetary Science Letters* 471: 125–35.

Sossi, P. A., Nebel, O., and Foden, J. 2016. Iron Isotope Systematics in Planetary Reservoirs. *Earth and Planetary Science Letters* 452: 295–308.

van den Boorn, S. H. J. M., Vroon, P. Z., and van Bergen, M. J. 2009. Sulfur-Induced Offsets in MC-ICP-MS Silicon-Isotope Measurements. *Journal of Analytical Atomic Spectrometry* 24: 1111–4.

Wade, J., and Wood, B. J. 2005. Core Formation and the Oxidation State of the Earth. *Earth and Planetary Science Letters* 236: 78–95.

Wang, K., Moynier, F., Barrat, J.-A., Zanda, B., Paniello, R. C., and Savage, P. S. 2013. Homogeneous Distribution of Fe Isotopes in the Early Solar Nebula. *Meteoritics & Planetary Science* 48: 354–64.

Wang, K., Moynier, F., Dauphas, N., Barrat, J. A., Craddock, P. R., and Sio, K. 2012. Iron Isotopic Compositions of Angrites and Stannern-Trend Eucrites. *Lunar and Planetary Science Conference*, LPI contribution No. 1659, 1146.

Wang, K., Savage, P. S., and Moynier, F. 2014. The Iron Isotope Composition of Enstatite Meteorites: Implications for their Origin and the Metal/Sulfide Fe Isotopic Fractionation Factor. *Geochimica et Cosmochimica Acta* 142: 149–65.

Wasson, J. T., Kallemeyn, G. W., Runcorn, S. K., Turner, G., and Woolfson, M. M. 1988. Compositions of Chondrites. *Philosophical Transactions of the Royal Society of London. Series A: Mathematical and Physical Sciences* 325: 535–44.

Weisberg, M. K., Bunch, T. E., Wittke, J. H., Rumble, I. D., and Ebel, D. S. 2012. Petrology and Oxygen Isotopes of NWA 5492, a New Metal-Rich Chondrite. *Meteoritics & Planetary Science* 47: 363–73.

Weisberg, M. K., Ebel, D. S., Nakashima, D., Kita, N. T., and Humayun, M. 2015. Petrology and Geochemistry of Chondrules and Metal in NWA 5492 and GRO 95551: A New Type of Metal-Rich Chondrite. *Geochimica et Cosmochimica Acta* 167: 269–85.

Weisberg, M. K., and Kimura, M. 2012. The Unequilibrated Enstatite Chondrites. *Geochemistry* 72: 101–15.

Weyer, S., Anbar, A. D., Brey, G. P., Münker, C., Mezger, K., and Woodland, A. B. 2005. Iron Isotope Fractionation during Planetary Differentiation. *Earth and Planetary Science Letters* 240: 251–64.

Weyer, S., and Ionov, D. A. 2007. Partial Melting and Melt Percolation in the Mantle: The Message from Fe Isotopes. *Earth and Planetary Science Letters* 259: 119–33.

Weyrauch, M., Horstmann, M., and Bischoff, A. 2018. Chemical Variations of Sulfides and Metal in Enstatite Chondrites—Introduction of a New Classification Scheme. *Meteoritics & Planetary Science* 53: 394–415.

Williams, H. M., Markowski, A., Quitté, G., Halliday, A. N., Teutsch, N., and Levasseur, S. 2006. Fe Isotope Fractionation in Iron Meteorites: New Insights into Metal-Sulphide Segregation and Planetary Accretion. *Earth and Planetary Science Letters* 250: 486–500.

Wood, B. J., Walter, M. J., and Wade, J. 2006. Accretion of the Earth and Segregation of its Core. *Nature* 441: 825–33.

Young, E. D., Manning, C. E., Schauble, E. A., Shahar, A., Macris, C. A., Lazar, C., and Jordan, M. 2015. High-Temperature Equilibrium Isotope Fractionation of Non-Traditional Stable Isotopes: Experiments, Theory, and Applications. *Chemical Geology* 395: 176–95.

Zambardi, T., and Poitrasson, F. 2011. Precise Determination of Silicon Isotopes in Silicate Rock Reference Materials by MC-ICP-MS. *Geostandards and Geoanalytical Research* 35: 89–99.

Zambardi, T., Poitrasson, F., Corgne, A., Méheut, M., Quitté, G., and Anand, M. 2013. Silicon Isotope Variations in the Inner Solar System: Implications for Planetary Formation, Differentiation and Composition. *Geochimica et Cosmochimica Acta* 121: 67–83.

Zhang, B. 2014. Calculation of Self-Diffusion Coefficients in Iron. *AIP Advances* 4: 017128.

Zhu, X. K., Guo, Y., O'Nions, R. K., Young, E. D., and Ash, R. D. 2001. Isotopic Homogeneity of Iron in the Early Solar Nebula. *Nature* 412: 311–3.

Ziegler, K., Young, E. D., Schauble, E. A., and Wasson, J. T. 2010. Metal–Silicate Silicon Isotope Fractionation in Enstatite Meteorites and Constraints on Earth's Core Formation. *Earth and Planetary Science Letters* 295: 487–96.

## APPENDIX A

## $\Delta^{30}$SI OF $SIO_{(GAS)}$ IN THE EC-FORMATION REGION

The $\delta^{30}$Si value of $SiO_{(gas)}$ was calculated considering the following parameters:

- $\delta^{30}$Si of the silicate phases (composed predominantly of enstatite) of unequilibrated enstatite chondrites: $-0.43 \pm 0.25$‰ (This study + Literature Data).
- Average formation temperature of EH chondrite: $980 \pm 150$ K.

The equilibrium isotopic fractionation factor as a function of temperature $T$ (K) for $T > 500$ K is given by Equation (A1):

$$1000 \times \ln(\alpha) = axu + bxu^2 + cxu^3, u = 10^6/T^2 \quad \text{(A1)}$$

The coefficients of the polynomial fit for $^{30}Si/^{28}Si$ isotope fractionation between enstatite and $SiO_{(gas)}$ as a function of temperature are as follows (Javoy et al., 2012):

| *a* | *b* | *c* |
|---|---|---|
| 4.1877 | −0.056078 | −0.0002044 |

Considering the coefficient values and the average temperature of EH in Equation (A1), we get

$$\delta^{30}Si_{Enstatite} - \delta^{30}Si_{SiO} = 4.1877 \times \frac{10^6}{(980 \pm 150)^2} - 0.056078 \times \left(\frac{10^6}{(980 \pm 150)^2}\right)^2 - 0.0002 \times \left(\frac{10^6}{(980 \pm 150)^2}\right)^3$$

Putting the $\delta^{30}Si$ of the silicate phases of EH3 chondrites and rounding off, we get

$$\delta^{30}Si_{SiO} = -4.8 \pm 0.6‰$$

## APPENDIX B

## CONDENSATION TEMPERATURE OF METALS IN EC-FORMATION REGION

The condensation temperature of metals in EC-forming region was calculated considering the following parameters:

$$\delta^{30}Si_{SiO} = -4.8 \pm 0.6‰$$

Average $\delta^{30}Si$ of bulk metals of EH3 chondrite: $-6 \pm 0.3‰$.

Average temperature of EH chondrite: $980 \pm 150$ K.

The coefficients of the polynomial fit for $^{30}Si/^{28}Si$ isotope fractionation between FeSi and $SiO_{(gas)}$ as a function of temperature are as follows (Javoy et al., 2012):

| *a* | *b* | *c* |
|---|---|---|
| −1.7251 | 0.10443 | −0.0026672 |

Considering these coefficient values in Equation (A1), we get

$$\delta^{30}Si_{FeSi} - \delta^{30}Si_{SiO} = -1.7251 \times \frac{10^6}{T^2} + 0.10443 \times \left(\frac{10^6}{T^2}\right)^2 - 0.0026672 \times \left(\frac{10^6}{T^2}\right)^3$$

Substituting the values of $\delta^{30}Si_{FeSi}$ and $\delta^{30}Si_{SiO}$ in the above equation, we get

$$T_{FeSi} = 1200 \pm 200 \text{ K}$$

## APPENDIX C

## CONDENSATION TEMPERATURE OF $SiO_2$ IN EC-FORMATION REGION

The condensation temperature of $SiO_2$ was calculated assuming that white mineral phases (WMPs) of EH3 chondrites are the best representative of $SiO_2$ in the EC-forming region. The following parameters were taken into consideration.

$$\delta^{30}Si_{SiO} = -4.8 \pm 0.6‰$$

$\delta^{30}Si$ of WMP from Sahara 97072 = $+0.23 \pm 0.10‰$.

Average temperature of EH chondrite: $980 \pm 150$ K.

The coefficients of the polynomial fit for $^{30}Si/^{28}Si$ isotope fractionation between Quartz ($SiO_2$) and $SiO_{(gas)}$ as a function of temperature are as follows (Javoy et al., 2012):

| *a* | *b* | *c* |
|---|---|---|
| 4.6409 | −0.056228 | 0.00041 |

Considering these coefficient values in Equation (A1), we get

$$\delta^{30}Si_{Quartz} - \delta^{30}Si_{SiO} = 4.6409 \times \frac{10^6}{T^2} - 0.056228 \times \left(\frac{10^6}{T^2}\right)^2 + 0.00041 \times \left(\frac{10^6}{T^2}\right)^3$$

$$T_{SiO_2} = 960 \pm 50\text{K}$$